Contents lists available at ScienceDirect

LITHOS

journal homepage: http://ees.elsevier.com

Research article

The pyroclastic breccias from Cabezo Negro de Tallante (SE Spain): Is there any relation with carbonatitic magmatism?

Francesca Innocenzi [a], Sara Ronca [a], Samuele Agostini [b], Marco Brandano [a], Antonio Caracausi [c], Michele Lustrino [a,d,*]

[a] Dipartimento di Scienze della Terra, Sapienza Università di Roma, P.le A. Moro, 5, 00185 Roma, Italy
[b] Istituto di Geoscienze e Georisorse – CNR, Via Moruzzi, 1, 56124 Roma, Italy
[c] Istituto Nazionale di Geofisica e Vulcanologia, Sezione di Palermo, Via Ugo La Malfa, 153, 90146 Palermo, Italy
[d] Istituto di Geologia Ambientale e Geoingegneria – CNR, c/o Dipartimento di Scienze della Terra, Sapienza Università di Roma, P.le A. Moro, 5, 00185 Roma, Italy

ARTICLE INFO

Article history:
Received 10 December 2020
Received in revised form 24 March 2021
Accepted 25 March 2021
Available online xxx

Keywords
Carbonatite
Carbonate
Petrology
Calcrete
Subduction
Basaltic rocks

ABSTRACT

The small Plio-Quaternary volcanic centre of Cabezo Negro de Tallante in SE Spain includes a thick deposit of polymictic pyroclastic tuff-breccia, whose fragments are agglutinated by a carbonate-rich component. This feature is also observed in other monogenetic volcanic centres cropping out in the Tallante-Cartagena volcanic district. The carbonate fraction has been recently interpreted in literature as representing a mantle component, therefore pointing to the existence of a diffuse carbonatitic activity in the area.Based on detailed sedimentological (presence of pisoids and root remnants), petrographic (presence of plagioclase and absence of euhedral silicate minerals in the calcite plagues), mineral chemistry (Ba-Sr-poor calcite composition), whole-rock chemistry (overall low incompatible element content in the pure carbonate fraction and a monotonous trace element negative correlation with CaO) as well as isotopic constraints (perfect correlation between Sr-Nd-Pb isotopic ratios with CaO in the basaltic and carbonate fraction, as well as heavy $\delta^{18}O$ and light $\delta^{13}C$ isotopic composition of the carbonate fraction), we propose a secondary origin for the carbonate component, excluding any contribution of mantle carbonatite melts. The presence of carbonates infiltrating the abundant mantle and crustal xenolith fragments found in the pyroclastic breccia is not related to the presence of carbonatitic melts at mantle to lower crustal depths, but to in-situ fragmentation of the Strombolian tuff-breccia deposit, followed by secondary carbonate infiltration. The pyroclastic breccia was indeed affected by an alternation of carbonate precipitation and dissolution in a vadose zone, where the activity of bacteria, fungi, roots and meteoric water led to the formation of a calcrete (*caliche*)-type deposits.Basaltic rocks (hawaiites and basanites) occur in the area as scoria and lava fragments in the pyroclastic breccia as well as small lava flows. They have been modelled with a low-degree partial melting of an amphibole-bearing peridotitic mantle close to the lithosphere-asthenosphere boundary. The origin of the mildly alkaline sodic basaltic activity in SE Spain post-dates the abundant and long-lasting subduction-related volcanic phase in the Betic Chain. Its origin is explained without requiring the presence of any thermal anomaly, but simply as consequence of the difference of lithospheric depths and edge-driven-type small-scale convection.

1. Introduction

Carbonatite magmatism has attracted the interest of the researchers for more than 60 years (e.g., Lustrino et al., 2021; Wyllie and Tuttle, 1960; Yaxley et al., 2019). The origin of carbonatitic melts has been related to several processes, often interconnected, such as: 1) low-degree direct partial melting of a carbonated peridotitic mantle (e.g., Litasov and Shatskiy, 2018; Wallace and Green, 1988); 2) partial melting of carbonated eclogite (e.g., Poli, 2016); 3) unmixing from silicocarbonatite magma at mantle depths (e.g., Lee et al., 2000; Martin et al., 2013) or 4) prolonged fractionation of strongly evolved CO_2-rich melts (e.g., Schmidt and Weidendorfer, 2018; Tappe et al., 2017). Another possibility to form carbonatitic or "pseudocarbonatitic" magma is related to the digestion of marine and continental sedimentary carbonates by basic-ultrabasic melts and then unmixed at relatively shallow magma chamber depths (e.g., Gozzi et al., 2014; Hegner et al., 2020; Lustrino et al., 2019, 2020; Shaw, 2018).

The origin of the most abundant carbonatitic magma (Ca-carbonatites) is particularly puzzling. Indeed, despite experimental petrology

* Corresponding author at: Dipartimento di Scienze della Terra, Sapienza Università di Roma, P.le A. Moro, 5, 00185 Roma, Italy.
E-mail address: michele.lustrino@uniroma1.it (M. Lustrino)

https://doi.org/10.1016/j.lithos.2021.106140
0024-4937/

indicates dolomitic to magnesitic melts as the only carbonates in equilibrium with a peridotitic matrix, calcite carbonatites are considered the typical carbonate melts produced in the upper mantle at a depth ranging from ~60 to ~250 km (e.g., Hammouda and Keshav, 2015). The overall incompatible element budget of Ca-carbonatites, considered a key aspect in igneous petrogenesis (e.g., Woolley and Kempe, 1989) has been now reconsidered and strongly connected to the silicate magma associated to them (e.g., Nabyl et al., 2020).

In Spain, carbonatites or carbonatitic components have been reported in the Campo de Calatrava Volcanic Province (central Spain; e.g. Bailey et al., 2005; Humphreys et al., 2010; Stoppa et al., 2012) and in the Tallante-Cartagena area (SE Spain; Toscani et al., 2020). An alternative interpretation considers the calcium carbonate inclusions found in olivine of the Late Miocene Morron de Villamayor lavas (Campo de Calatrava Volcanic Province) as the result of a process of limestone digestion by a basic-ultrabasic magma (Lustrino et al., 2016). In the same way, the presence of carbonatitic melts in a small monogenetic volcano in SE Spain (Cabezo Negro de Tallante) associated to basaltic to hawaiitic compositions is here questioned. Based on a detailed volcanological, sedimentological, petrographic, mineral chemical, geochemical and isotopic (Sr-Nd-Pb-O-C) investigation, we propose for the carbonate component agglutinating the pyroclastic breccia of the Tallante-Cartagena area a sedimentary origin. The carbonate fraction is here classified as a caliche-calcrete deposit infiltrated after the emplacement of the pyroclastic succession, unrelated to any mantle carbonate component.

2. Geological background

The Alpine Tethys was completely subducted during early Eocene, as consequence of the counter-clockwise rotation of Africa and the partially coeval counter-clockwise rotation of Iberia triggered by the opening of the Bay of Biscay (Favre and Stampfli, 1992; Stampfli and Hochard, 2009; Stampfli and Kozur, 2006). The compressional regime associated to such oceanic subduction (the Eoalpine phase of the Alpine Orogeny) evolved into continental collision in the south-eastern margin of Iberia, leading to the formation of the NE-SW-directed Betic Chain. This is an orogenic belt with a length of ~600 km and maximum width of ~200 km, characterized by a NW-directed tectonic transport (Fig. 1a,b; Handy et al., 2010; Puga et al., 2011; Carminati et al., 2012; Faccenna et al., 2014; van Hinsbergen et al., 2020).

Since the Oligocene, a new extensional phase developed along eastern Iberia, leading to the Oligo-Miocene opening of the Alboran Sea and the Valencia Trough (Carminati et al., 2012; Casciello et al., 2015; Faccenna et al., 2014; Guerrera et al., 2019; Lustrino et al., 2009, 2011; van Hinsbergen et al., 2020). It occurred as consequence of the back-arc basin opening associated to another orogenetic phase (the Apennine-Maghrebide subduction), characterized by the flip of the oceanic subduction polarity from SE (Alpine subduction) towards NW (e.g., Carminati et al., 2012; Lustrino et al., 2009, 2017).

3. Campo de Cartagena

The Campo de Cartagena is one of the several sedimentary basins developed since late Miocene in the Eastern Betic strike-slip fault zone, where compressional and extensional structures coexist (Montenat and d'Estevou, 1999; Pedrera et al., 2010). This basin is part of the wider Alicante-Cartagena Basin, considered the northern prolongation of the Algerian Basin (Fig. 1b). The Campo de Cartagena is filled up with Neogene marls and Quaternary deposits, located in the south-eastern corner of Spain (Fig. 1b; Goy and Zazo, 1989; Dabrio et al., 1991; Vera, 2000). These sediments (siliciclastic and carbonate) were emplaced both in continental and marine environments (García-Hernández et al., 1980; Meijninger and Vissers, 2006; Sanz de Galdeano, 1990).

During the late Miocene, this area was characterized by the deposition of Messinian evaporites related to the Mediterranean salinity crisis (e.g., Sissingh, 2008; Soria et al., 2001). A transitional depositional environment developed during Plio-Quaternary in the basins of Lower Segura and Campo de Cartagena. These areas were characterized by a lagoon-barrier island transitional environment, also with an estuarine and a marshy plain with barrier islands (Bardaji et al., 1995; Goy et al., 1990). Here, fluvial sediments coming from the Guadalentin Depression and flowing towards the Mediterranean Sea, accumulated for a total thickness of ~150 m (Alonso-Zarza et al., 1998). The progradation of the Guadalentín River in the Campo de Cartagena led to the deposition of copious carbonates, derived mostly from the limestones cropping out in the external area of the Betic Chain (Subbetic Zone; Bardaji et al., 1995). The main deposits of the Campo de Cartagena were calcarenites and silts plus white limestones and marls (Bardaji et al., 1995). Successively, the middle Pleistocene tectonics generated a set of N-S trending normal faults that deformed the ancient fluvial systems, leading to the development of transverse alluvial fan systems fed by marginal reliefs (Alonso-Zarza et al., 1998; Silva et al., 1993). The Pleistocene alluvial fan surfaces are capped by thick mature calcretes, in some cases reaching a thickness of ~5 m, affecting also the former fluvial red paleosoils (Alonso-Zarza et al., 1998; Samoza et al., 1989).

4. Volcanic activity in SE Spain

In several central-western Mediterranean areas such as Spain, France, Morocco and Sardinia, two different magmatic phases are commonly recorded during the Cenozoic (e.g., Lustrino, 2000; Lustrino et al., 2011). The first phase developed mostly from Oligocene to Miocene, with igneous products showing orogenic geochemical signature related to the subduction-related modifications of their mantle sources (e.g., Conticelli et al., 2009; Coulon et al., 2002; Duggen et al., 2004, 2005; Gill et al., 2004; Lustrino et al., 2011; Turner et al., 1999). The second phase took place mostly during Plio-Quaternary. It is represented by much less widespread and smaller volume volcanic rocks, characterized by compositions showing anorogenic geochemical signature, with mostly mildly alkaline sodic lithologies (Cebriá et al., 2009; Duggen et al., 2005; Lustrino and Wilson, 2007).

In the area north-west of Cartagena, Plio-Pleistocene (2.9–2.3 Ma) volcanic rocks crop out near the village of Tallante. These products represent the youngest volcanic activity recorded in the SEVP. They are mainly hawaiites with minor basanites, commonly characterized by an abundant mantle xenolith cargo (Fig. 1c; Bellon et al., 1983; Beccaluva et al., 2004; Duggen et al., 2005; Lustrino and Wilson, 2007; Bianchini et al., 2011; Hidas et al., 2016; Manteca et al., 2016; Toscani et al., 2020). The eruptive style of the young products is moderately explosive, mainly Strombolian, with some phreatomagmatic events, as testified by the consistent pyroclastic deposits cropping out at some eruption centres in the area surrounding Tallante and Los Perez (i.e., Cabezo Negro de Tallante, Cabezo Negro de los Perez) and more southerly at Cabezo Negro de las Torres (Manteca et al., 2016). The pyroclastic products (poorly lithified lapilli tuffs and tuff breccias) rich in lithics such as lava and basement fragments are covered by thin lava flows (Cebriá et al., 2009; Romero and Belmonte, 2011; Toscani et al., 2020), with an overall alkali basaltic/hawaiitic composition, dated at ~2.9–2.3 Ma (Duggen et al., 2005; Toscani et al., 2020; Electronic Appendix 1). The repetition of the pyroclastic-effusive phases occurring in some vents suggests that the volcanic activity was characterized by multiple eruptive episodes (Manteca et al., 2016). An intense erosion has modified the original morphology, rendering the complete reconstruction of the volcanic history difficult, for the absence of preserved craters and the dismembering of the lava flows in discontinuous outcrops (Manteca et al., 2016).

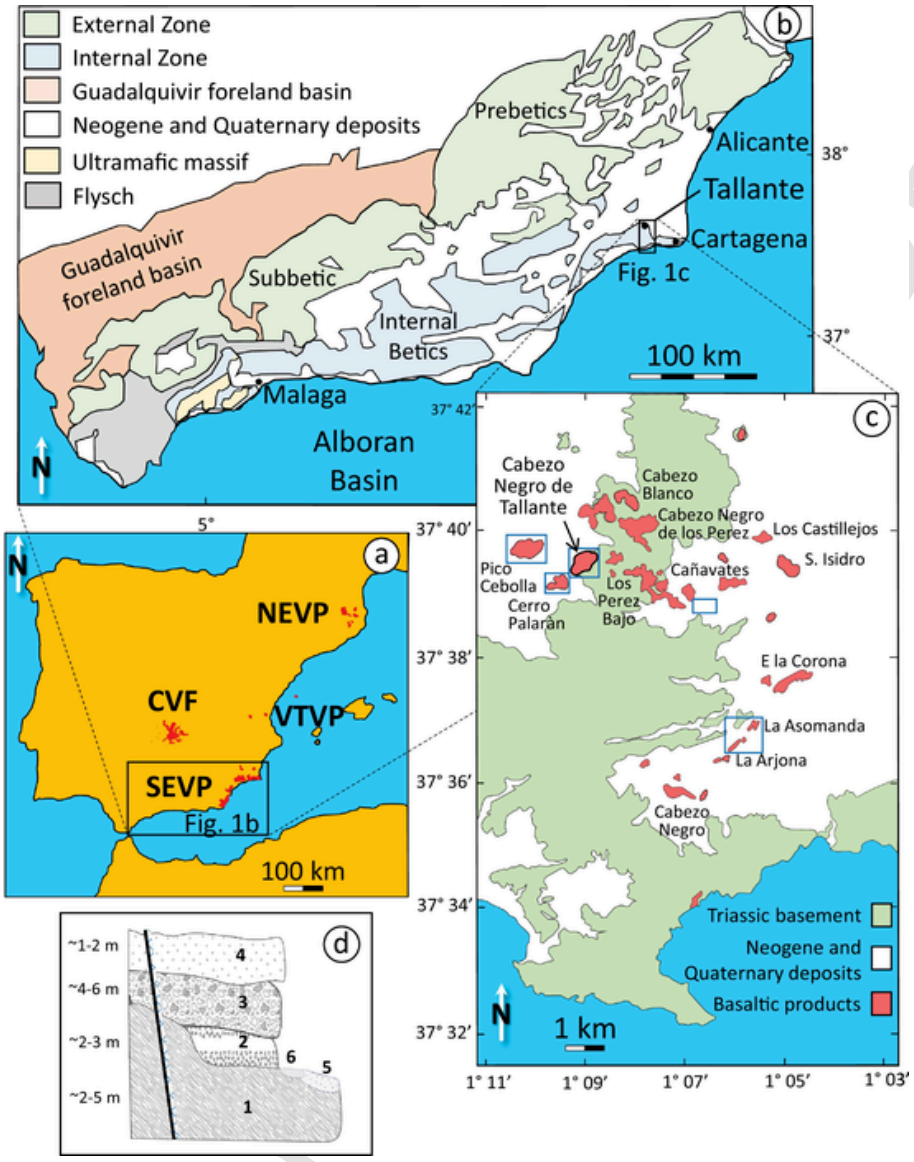

Fig. 1. (a) Volcanic provinces of Spain: CVF = Calatrava Volcanic Field, NEVP = North-East Volcanic Province, SEVP = South-East Volcanic Province, VTVP = Valencia Trough Volcanic Province. (b) Geological sketch map of the Betic orogenic belt, modified after Bianchini et al. (2011). (c) Distribution of the basaltic igneous products in the Tallante area. Modified after Cebriá et al. (2009). Blue squares highlight the main sampling sites of this study. (d) Stratigraphic sketch of Cabezo Negro de Tallante volcano. The thickness of the strata is only qualitative, as estimated during the fieldwork. 1: metamorphic basement (silvery-grey micaschists, bluish green chloritoid-bearing schists and quartz schists; Nevado-Filabride complex; age of protolith Paleozoic-Triassic, alpine metamorphism), 2: poorly sorted and weakly consolidated pyroclastic deposit (Plio-Pleistocene), 3: Strombolian pyroclastic tuff-breccia deposit (Plio-Pleistocene), 4: alkali basalt lava flow (Plio-Pleistocene), 5: alluvial fan deposits (Late Pleistocene), 6: colluvial deposits (Late Pleistocene-Holocene). The black line is a rough representation of the dike, while the small blue crosses close to it represent the associated metamorphic component. (For interpretation of the references to colour in this figure legend, the reader is referred to the web version of this article.)

The Plio-Pleistocene alkali basaltic/hawaiitic rocks from the area of Cartagena show geochemical features coherent with the worldwide intracontinental alkali basalts. Cebriá et al. (2009) proposed a sub-lithospheric mantle as the source for these basaltic rocks and a subsequent interaction with melts produced by the overlying lithospheric mantle metasomatized during the previous subduction tectonics. According to Toscani et al. (2020), the emplacement of the carbonate component of the pyroclastic breccia cropping out at Cabezo Negro de Tallante is synchronous with the silicate magma production, as consequence of a liquid immiscibility at relatively shallow depths. Toscani et al. (2020) consider the high content of CO_2 is the cause of the explosive activity of Cabezo Negro de Tallante.

5. Macroscopic description, petrography and mineral chemistry

Only a brief description on the sampling sites, of the macroscopic and microscopic features of the samples and of the main mineral chemical characters is presented here. Details on all these aspects are reported in Electronic Appendix 1 (sampling sites), Electronic Appendix 2 (hand-specimen description), Electronic Appendix 3 (petrography), Electronic Appendixes 4a and 4b (mineral and glass chemistry).

5.1. Sampling localities

The sampling sites of the thirty-nine samples collected in the Campo de Cartagena volcanic district in November 2019 are reported in detail in the Electronic Appendix 1. Twenty-six samples are from Cabezo Negro de Tallante (Fig. 1 of Electronic Appendix 1), with the remaining

coming from neighbouring volcanic centres (e.g., Pico Cebolla) and small lava flows (e.g., Peñas Blancas; Figs. 10 and 11 of Electronic Appendix 1).

Four samples are thin hardened carbonate crusts (calcrete), sixteen samples are pyroclastic breccias (with block- lapilli- and ash-sized fragments) and lapilli tuff deposits, and eight samples are massive to scoriaceous lava flows. These have been collected in nearly all the different localities, with calcretes found both covering pyroclastic breccia as well as some massive lava flows (Fig. 2a). One sample of nodular calcrete, two dense dark-coloured cumulate samples, as well as one mantle and two crustal xenoliths, one amphibole xenocryst, one felsic vitrophyric sample and three samples from the Betic metamorphic basement complete the collection.

Cabezo Negro de Tallante covers a metamorphic basement, represented by the Nevado-Filabride complex (Augier and Jolivet, 2005) locally consisting of silvery grey mica-schists, quartz-schists and quartzites. The lowermost unit of the volcanic succession (Fig. 4 of Electronic Appendix 1) recognised in the area of Cabezo Negro de Tallante is a poorly consolidated, reddish brown primary volcaniclastic (pyroclastic) deposit, a few meters thick, mainly composed of lapilli and volcanic ash (Toscani et al., 2020). The pyroclastic deposit, cropping out along the southern and eastern slope of the hill, consists of an alternation of ~20 cm-thick massive strata, with planar or low angle cross-lamination and thinner, slightly coarser-grained, layers with high angle cross-lamination. In some parts, the deposit is more chaotic and

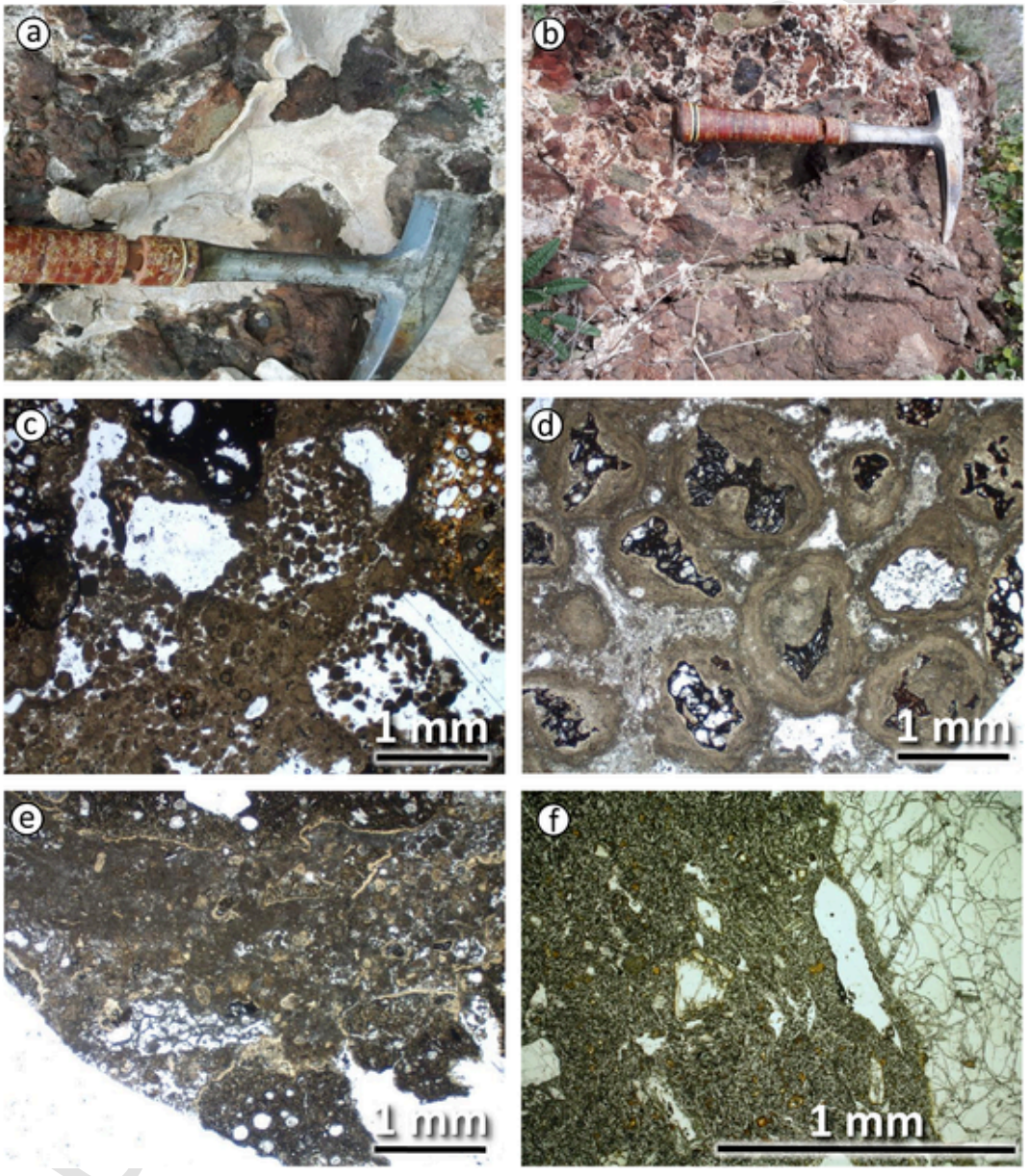

Fig. 2. (a) Superficial hardened crust of carbonate (i.e., calcrete) that covers the pyroclastic breccia deposit in the Cabezo Negro de Tallante. (b) Outcrop of Strombolian pyroclastic breccia deposit in Cabezo Negro de Tallante volcanic center. (c) Optical microscope thin-section micrograph of pyroclastic breccia sample, TAF5, in plane-polarized light (PPL). Black and yellow volcanic scoriae in a heterogeneous carbonate matrix. The matrix shows a clotted fabric, with peloids. (d) Optical microscope thin-section micrograph of pyroclastic breccia sample, TAF6, at PPL. Pisoids, made of concentric carbonate laminae precipitated around former grains as black scoriae. (e) Optical microscope thin-section micrograph of pyroclastic breccia sample, TAF32, at the PPL. Black scoriae in a carbonate matrix characterized by a clotted fabric with peloids and rhizoliths. (f) Optical microscope thin-section micrograph of a basaltic lava sample, TAF23, at the PPL. A porphyritic lava with phenocrysts of olivine and clinopyroxene set in a hypocrystalline groundmass made of microliths of plagioclase, olivine and clinopyroxene. A mantle xenolith is also present. (For interpretation of the references to colour in this figure legend, the reader is referred to the web version of this article.)

poorly sorted, including some coarse-sized basement xenoliths and scoriae. It is pervaded by a network of carbonate veins.

The overlying unit, the main object of this study, consists of massive pyroclastic breccias (Fig. 2b) and medium to coarse-grained lapilli tuffs agglutinated by a whitish carbonate matrix, which ranges from ~20 to 40% in volume (Figs. 6 and 7 of Electronic Appendix 1). This deposit is composed of a poorly sorted and clast- to matrix-supported mixture of fragments, angular to slightly rounded in shape, varying in size from <0.5 to >10 cm grouped under the lapilli, blocks, ash, and scoria grain-size classes. The fragments are both juveniles (volcanic scoriae and crystals) and lithics (blocks of lava, peridotite, pyroxenite and crustal xenoliths). No large pumices nor bombs have been found. Hereafter, the collective term "pyroclastic breccia" is used to collect all the volcanological facies variants (from medium lapilli-tuff to breccia).

Climbing towards the top of the Cabezo Negro de Tallante on the NE slope, a rocky spur resembling a dyke, characterized by sub-vertical or high-angle SE-dipping platy jointing structures (direction 41–221; dip 131/79, 121/89), clearly emerges from the pyroclastic breccia deposit. Numerous veins of quartz, ~0.5–2 cm thick, occur in this rock, and calcite veins in turn crosscut them (Fig. 9 of Electronic Appendix 1). Some kinematic indicators (S—C surfaces) suggest a sinistral sense of shear. Many portions of the rock mass exhibit features macroscopically similar to the rheomorphic structures developing in high viscosity magmas and/or to those observable in mylonitic rocks. Toscani et al. (2020) considered this outcrop as the basaltic feeding dyke of the Cabezo Negro de Tallante, an interpretation at odds with our findings. The vegetation and the breccia deposit all around the outcrop prevent a complete understanding of the lithologic and stratigraphic relationships.

The volcanic succession ends with a porphyritic lava flows characterized by the presence of mantle and crustal xenoliths with a maximum size of ~25 cm. The thickness of lava flows is highly variable, ranging from <1 m in some parts of the Cabezo Negro to >10 m in the remains (close to Fuente Vieja) of the small lava flows of Cabezo Negro de Las Torres (Electronic Appendix 1; Manteca et al., 2016).

5.2. Petrography

The petrography of the 39 collected samples is briefly reported below, with details fully described in Electronic Appendix 3. Carbonate deposits in the form of calcrete are widespread in all the investigated area. All occur as indurated and highly heterogeneous whitish carbonate superficial crusts, matrix-supported with a mudstone to wackestone texture. The fine-grained cemented carbonate constitutes more than 90% of the total volume of the rocks and encloses non-carbonate grains such as schistose lithic fragments and monocrystalline grains (Fig. 1a and b of Electronic Appendix 3). The micrite matrix is heterogeneous, characterized by both wavy micro-laminar and nodular fabric in the same sample. Seldom it shows tiny acicular crystals of calcite that outline rhizoliths, i.e. traces of roots left by the cementation and recrystallization of the former structures (Fig. 1c, d, g and h of Electronic Appendix 3).

The pyroclastic lapilli tuff unit is a massive to bedded, poorly sorted and moderately indurated deposits. It consists of glassy shards, microliths of plagioclase, clinopyroxene and mica, as well as lithic fragments of variable compositions (crustal xenoliths, scoriae, lava fragments; Fig. 2 of Electronic Appendix 3). The scoriae contain occasionally olivine, plagioclase and clinopyroxene phenocrysts in a groundmass made up of subhedral to euhedral plagioclase, subhedral clinopyroxene and anhedral quartz xenocrysts, platy white mica and subhedral amphibole.

Heterometric and polymictic pyroclastic breccias, moderately agglutinated by a carbonate matrix, are extremely diffuse in the area and all share similar petrographic features (Fig. 2c-e). They vary from matrix- to clast-supported and show a poor sorting, coupled with evidence of in-situ brecciation. About 80% of the clasts is represented by volcanic scoriae, yellow to brown in plane polarized light, while the rest is made of mantle and crustal xenoliths. The scoriae contain subhedral plagioclase, elongated clinopyroxene and anhedral to euhedral olivine phenocrysts set in a groundmass made up of the same phases plus opaque minerals and occasional glassy patches (Figs. 3 and 4 of Electronic Appendix 3). The carbonate matrix of the breccias is quite variable, consisting of micrite with floating mm-sized peloids (Fig. 3c and d of Electronic Appendix 3), coated grains (concentric laminae of carbonate covering the scoriae; Fig. 3e and f of Electronic Appendix 3) and laminar micrite. This is characterized by wavy lamination sometime coupled with concentric banded filling of the scoria vesicles. The clotted fabric of this micrite is definitely similar to that of calcrete.

Lava samples are dark grey porphyritic rocks with 15–25% commonly isooriented and empty vesicles (Fig. 2f). The phenocryst load rarely exceeds 15% in volume, set in a groundmass of iddingsitised subhedral olivine, euhedral plagioclase, euhedral to subhedral clinopyroxene, opaques minor volcanic glass and rare intergranular alkali-feldspar (Fig. 6 of Electronic Appendix 3). The phenocrysts are essentially euhedral to subhedral olivine (~90% of the phenocrysts), often with thin iddingsite rim, with minor subhedral zoned clinopyroxene and euhedral to anhedral plagioclase. Mantle and crustal xenoliths and xenocrysts are relatively common.

Ultramafic cumulates (Fig. 5 of Electronic Appendix 3) are amphibole-bearing pyroxenites. The main components, from ~0.1 to ~6 mm in size, are pleochroic brown to pale yellow, anhedral and poikilitic Ca-amphibole (~50–70%) together with anhedral clinopyroxene showing thin orthopyroxene exsolution lamellae, orthopyroxene and biotite, euhedral olivine, labradoritic plagioclase and opaque crystals.

Mantle xenoliths of Cabezo Negro de Tallante are well known in literature, found both in the pyroclastic breccias and in the basaltic lavas (Fig. 7 of Electronic Appendix 3). The xenoliths have angular to sub-

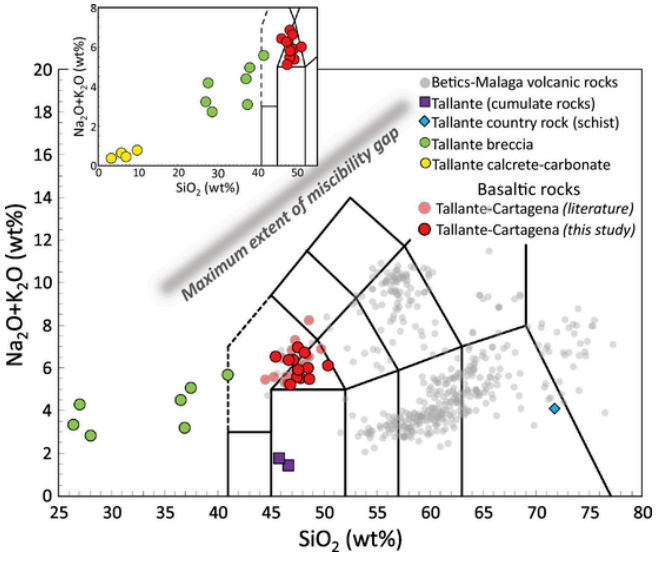

Fig. 3. Total alkali vs. silica (TAS diagram; Le Maitre, 2002) for the basaltic samples of Tallante area. Cumulates, country rock schist (TAF26), carbonate fraction of the breccia, calcrete and whole-rock pyroclastic breccia compositions, as well as the data for Tallante-Cartagena (Beccaluva et al., 2004; Capedri et al., 1989; Cebriá et al., 2009; Duggen et al., 2005; Turner et al., 1999) and Betic-Malaga (Nixon et al., 1984; Venturelli et al., 1984; Munksgaard, 1984; Torres-Roldán et al., 1986; Nelson et al., 1986; Toscani et al., 1990, 1995; Contini et al., 1993; Fernández Soler, 1996; Zeck et al., 1999; Benito et al., 1999; Duggen et al., 2004; Conticelli et al., 2009; Pérez-Valera et al., 2013; Mattei et al., 2014; Lustrino et al., 2016) are also plotted for comparison. The maximum extent of carbonatite-silicate melt miscibility gap is reported as a grey line (Schmidt and Weidendorfer, 2018). See discussion for further details.

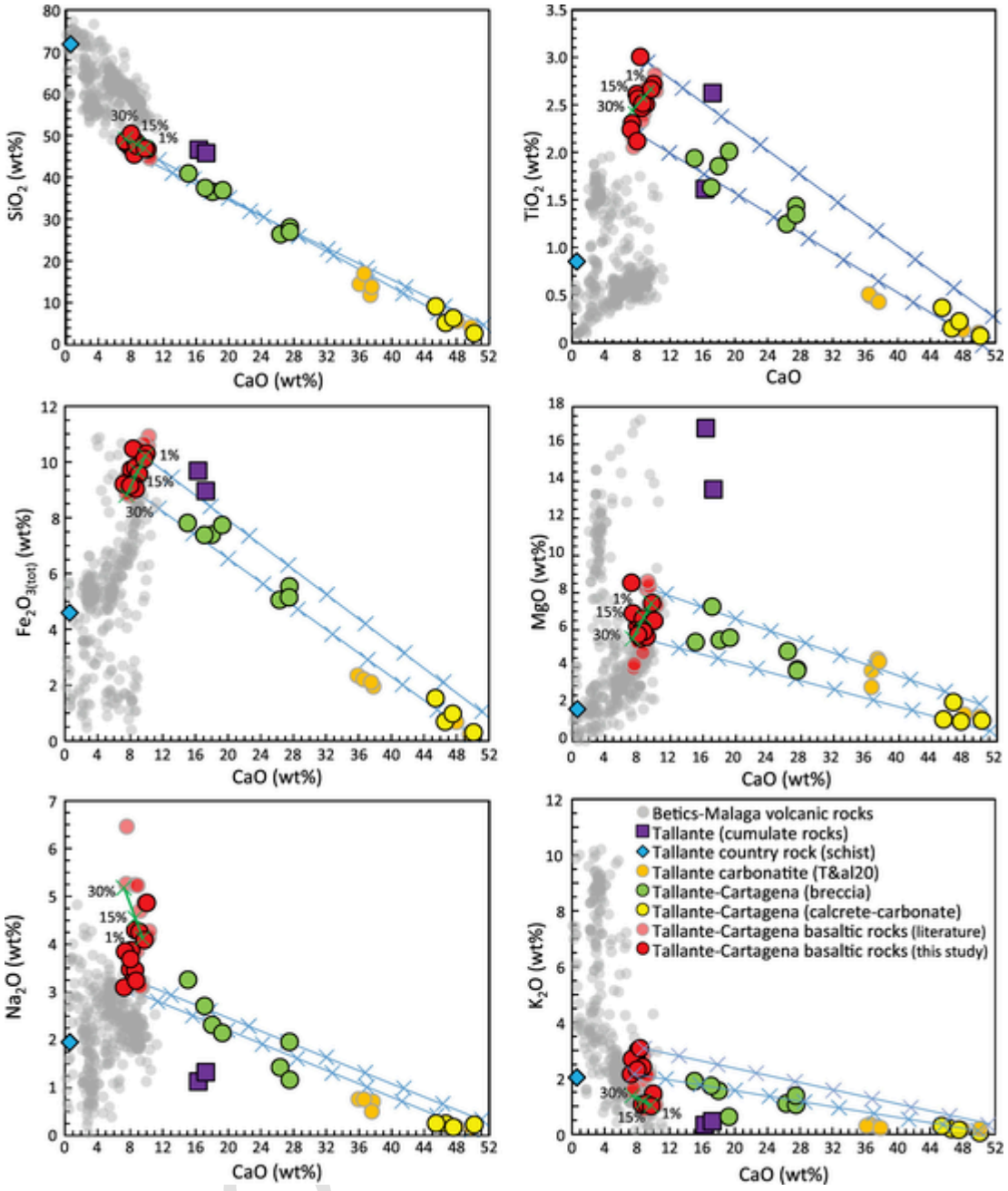

Fig. 4. SiO_2, TiO_2, Fe_2O_{3tot}, MgO, Na_2O and K_2O vs. CaO diagrams for Tallante rocks investigated in this study. References for Tallante-Cartagena basaltic rocks and for Betic-Malaga volcanic rocks are reported in the caption of Fig. 3. The compositions identified as carbonatite and *caliche*-type deposits by Toscani et al. (2020) are also plotted (T&al20). The two blue lines indicate mixing between the least evolved basaltic sample (TAF25S) and an "impure" carbonate (SiO_2 = 3.0 wt%, TiO_2 = 0.0 wt%, Al_2O_3 = 0.5 wt%, Fe_2O_3 = 0.2 wt%, MnO = 0.0 wt%, MgO = 2.0 wt%, CaO = 50.0 wt%, Na_2O = 0.1 wt%, K_2O = 0.1 wt%, P_2O_5 = 0.05 wt%) and mixing between the most evolved basaltic sample (TAF17) and a hypothetically pure limestone (CaO = 56 wt%). The complete list of major oxide diagrams vs. CaO, SiO_2 and MgO is reported in Electronic Appendix 6. (For interpretation of the references to colour in this figure legend, the reader is referred to the web version of this article.)

angular shapes, reach up to ~25 cm in size and show an overall lherzolitic modal composition. Fine- to medium-grained (crystal size ranging from ~0.3 to ~4.3 mm) mafic rock xenoliths with leuconorite composition show metamorphic re-crystallization with granoblastic microstructure. Metasedimentary lithic grains are present in most of studied samples, represented by fine-grained, often schistose, low-grade metarenitic to metapelitic rocks composed of quartz + plagioclase + epidote + white mica + chlorite + tourmaline ± biotite and less frequently by quartzite (Fig. 8 of Electronic Appendix 3). In the north-eastern sector of the Cabezo Negro de Tallante, strongly deformed metasedimentary schistose rocks crop out. These rocks, mostly consisting of quartz, feldspars, opaques and very fine-grained mica, display a protocataclastic-protomylonitic fabric with the mylonitic foliation cross-cutting the main schistosity, also with porphyroclasts of quartz and feldspar (Fig. 9 of Electronic Appendix 3).

A heterogeneous volcanic felsic rock rich in metasedimentary fragments has been sampled in contact with highly deformed quartz-schists from what has been defined as the basaltic feeding dyke by Toscani et al. (2020). The metamorphic xenoliths are less than 5 mm in size and consist of partially or entirely opacitised schistose grains and fractured quartz-feldspatic granoblastic aggregate (Fig. 10 of Electronic Appendix 3). The whole-rock chemical composition of this sample has not

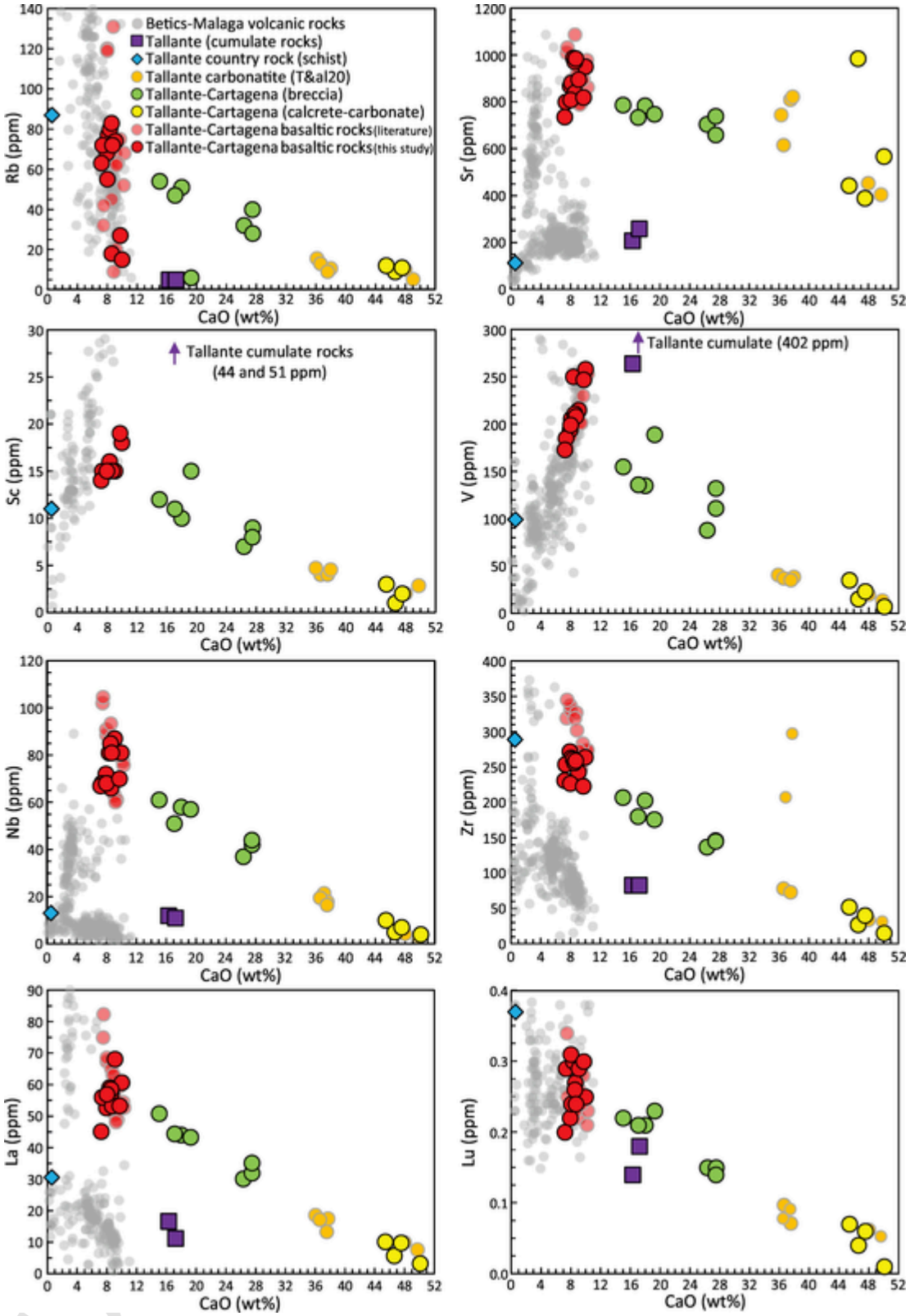

Fig. 5. Rb, Sr, Sc, V, Nb, Zr, La and Lu vs. CaO diagrams for Tallante rocks investigated in this study. References for Tallante-Cartagena basaltic rocks and for Betic-Malaga volcanic rocks are reported in the caption of Fig. 3. The Rb, Sc, V, Zr and La content of the Betics lamproites reaches 800 ppm, 40 ppm, 320 ppm, 1000 ppm and 90 ppm, respectively. The complete list of trace element diagrams vs. CaO, SiO_2 and MgO is reported in Electronic Appendix 6.

been analysed because of the impossibility to remove all these fragments from the igneous component. The volcanic rock groundmass is hypohyaline with elongated sanidine microliths (~0.1 mm) with swallow-tail terminations, likely associated to quenching. The glass shows a perlitic structure and the small vesicles are partially filled by acicular zeolites.

5.3. Mineral chemistry

Nineteen samples have been selected for SEM and EPM analyses (details in Electronic Appendixes 4a and 4b). Olivine has a forsterite content in the 68.8–86.5 mol% range and larnite content lower than 0.7 mol% (CaO 0.07–0.52 wt%; average 0.31 wt% Fig. 1 of Electronic Appendix 4a). Groundmass crystals cluster towards FeO-rich compositions. Olivine in the mantle xenoliths shows much narrower range and higher forsterite ($Fo_{89.4–90.5}$) as well as lower CaO (0.00–0.12 wt%; average 0.06 wt%) than magmatic olivine. Olivine in the ultramafic and pyroxenitic cumulates has moderate Fo content ($Fo_{75.1–75.5}$) and very low CaO (~0.08–0.09 wt%).

Clinopyroxene is a ubiquitous phase in the basaltic rocks, like olivine. Nearly all the compositions fall in the diopside field with minor augite, with minor changes between groundmass and phenocryst phases ($Wo_{45-57}En_{36-50}Fs_{1–12}$; Fig. 4 of Electronic Appendix 4a).

Plagioclase has been found in all the basaltic rock samples. It shows andesine to labradorite composition ($An_{31-66}Ab_{31-56}Or_{1–12}$) without differences in the scoria and massive lava flows, while plagioclase in the ultramafic cumulates is andesine ($An_{46}Ab_{51}Or_4$; Fig. 8 of Electronic Appendix 4a). Sanidine has been found in some segregation pockets occurring in one basaltic scoria (TAF24) and in the felsic vitrophyric sample forming the previously defined "basaltic feeding dyke" (Toscani et al., 2020) in Cabezo Negro de Tallante. It shows Na-rich compositions ($An_1Ab_{44-45}Or_{54–58}$), particularly relevant in the holocrystalline segregation pockets ($An_{2-6}Ab_{44-52}Or_{43–51}$; Fig. 8 of Electronic Appendix 4a).

Opaque oxides are present exclusively as groundmass phases in the volcanic scoria, but are also found in crustal and mantle xenoliths. Groundmass opaques belong to the rhombohedral phase solid solution, being rich in TiO_2 (36.1–42.0 wt%) and of FeO_{tot} (41.0–45.9). The oxides in the crustal xenoliths have even higher TiO_2 (50.2 wt%) but lower FeO_{tot} (35.8 wt%).

Carbonate from the matrix of the breccia and from calcrete-type hardened crust is calcite with a content of CaO varying from 48.0 to 58.2, low FeO (<0.6 wt%) and low MgO (0.4–3.2 wt%). Only for the inner core of a concentrically-banded replenishment of vesicles in basaltic scoria (TAF6), MgO in carbonate reaches higher contents (7.24–19.17 wt%). SrO and BaO contents are always low (average 0.09 and 0.02 wt%, respectively).

Analyses of glasses were carried out in the freshest portions of the basaltic volcanic scoriae embedded in the breccias, in the massive lavas and in the felsic vitrophyric "dyke" sample. The glasses in the basaltic samples cluster in two groups, one Ti-Fe-Mn-Mg-Ca-K rich and Na-poor, and the other with opposite characteristics. The overall SiO_2 range of basaltic glass is 45.6 to 55.6 wt%, with the samples richest in SiO_2 (53.2–55.6 wt) showing the lowest total (90.9–91.7 wt%; Fig. 11 of Electronic Appendix 4a). The alkali content ($Na_2O + K_2O$ = 6.9–11.6 wt%) monotonously increases with SiO_2 (R^2 = 0.81), corresponding to tephritic to tephriphonolitic compositions. The few glass analyses of the felsic vitrophyric sample show very low MgO (<0.07 wt) and very high SiO_2 (75.2–75.6 wt%), coupled with moderately high $Na_2O + K_2O$ (8.0–9.0 wt%), falling in the rhyolite field in the TAS diagram. The glass from reaction rims around quartz xenocrysts span a very variable chemical range, from rhyolitic, to phonolitic and trachyandesitic compositions (SiO_2 = 56.8–74.6 wt%; $Na_2O + K_2O$ = 9.9–12.8 wt%).

6. Whole-rock geochemistry

Nineteen samples have been selected for whole-rock geochemical study after a detailed petrographic selection. For one breccia (TAF32) it has been possible to separate the carbonate from the basaltic fraction by mechanical and chemical separation techniques. Thus, for this sample, three different aliquots have been analysed, one on the whole rock (with the suffix WR = whole rock), one on the carbonate fraction (with the suffix C = carbonate) and one on the basaltic fraction (with the suffix S = silicate). For another breccia (TAF5) we have separated three aliquots, one with the basaltic fraction only, and two with different carbonate/basaltic fragment ratios, reported as WR1 and WR2 in Table 1 (and Electronic Appendix 6). For other two breccias (TAF12 and TAF25), we have separated the basaltic fraction (reported as TAF12S and TAF25S) by removing with strong HCl the carbonate component and an aliquot representing the carbonate + basaltic components (reported as TAF12WR and TAF25WR). For two breccias (TAF27 and TAF37) we have analysed only the whole-rock analyses (i.e., mixed carbonate + basaltic components, reported as TAF27WR and TAF37WR). A careful handpicking under the binocular has removed all the exotic fragments (xenocrysts and xenoliths, as well as antecrysts and cognate nodules in the form of cumulate mafic-ultramafic lithologies) from the breccia. However, it is possible that the tiniest portions external to the basaltic rock-carbonate system could have left in the chips that were eventually pulverized and analysed. We are confident that the influence of these xenoliths and xenocrysts have only minimal effect on the whole-rock chemistry of the pyroclastic breccia.

Eight lavas (TAF8, TAF17, TAF23, TAF29, TAF30, TAF31, TAF34 and TAF36), two cumulate xenoliths (TAF4 and TAF11), one basement schist (TAF26), and three calcrete samples (TAF1, TAF28 and TAF38), the latter three labelled with the suffix "WR", complete the set of the analyses, summing up to 26 different aliquots from nineteen samples (Table 1). More details about the preparation and methods are reported in Electronic Appendix 5.

The whole-rock composition for all the investigated aliquots, together with literature data for the Tallante volcanic rocks and those from the Betics and Malaga areas are shown in Harker-type diagrams using CaO as abscissa. The complete dataset, including literature data and the diagrams is reported in Electronic Appendix 6. The choice of CaO as discrimination parameter is based on the extremely wide range (0.6–50.1 wt%) and because it can be a good tracer of mixing between carbonate and silicate rocks. In this way, it is possible to compare the almost pure carbonate aliquots (calcrete and carbonate portion of the breccias) with the mixed compositions and the basaltic portion of the breccias. The calcrete composition (sample TAF1, TAF28 and TAF38) has been used as a reference for the values of the sedimentary carbonate, while average Ca-carbonatite (Chakhmouradian, 2006; Woolley and Kempe, 1989) and average volcanic carbonatite estimates (Stoppa et al., 2016) are used as a reference for carbonatitic magma composition.

6.1. Major oxides

The lavas and the silicate fraction of the breccias (hereafter collectively reported as basaltic rocks) have SiO_2 content spanning a relatively small range, from ~45.4 to ~50.4 wt%, with a total alkali content ranging from ~4.1 to ~7.9 wt% (Table 1). In the TAS diagram (Le Maitre, 2002; Fig. 3), they straddle the trachybasalt-basanite fields (red circles) and overlap the Tallante literature data field (pink circles). The rocks plotting in the trachybasalt field should be distinguished into hawaiites and potassic trachybasalts according to their $(Na_2O\text{-}2.0)/K_2O$ ratios. Only a few of basaltic rocks (TAF23, TAF29, TAF30 and TAF36) plot in the sodic alkaline definition as proposed by IUGS [$(Na_2O\text{-}2.0)/K_2O \geq 1$], with the remaining samples showing $(Na_2O\text{-}2.0)/K_2O$ = 0.43–0.75. Being the Na_2O/K_2O ratio always >1 (1.1–4.0) we will adopt for these rocks the adjective "sodic" instead of "sodic" and "potassic". Consequentially, also the rocks that should be classified as potassic trachybasalts according to the IUGS rules are here classified as hawaiites.

Table 1
Major oxide and trace element content of Tallante area volcanic, sedimentary and metamorphic rocks. WR = Whole rock; S = Silicate portion of the pyroclastic breccia; C = Carbonate portion of polymictic carbonated breccia and calcrete.

Sample	Locality	SiO_2	TiO_2	Al_2O_3	Fe_2O_3	MnO	MgO	CaO	Na_2O	K_2O	P_2O_5	L.O.I	CO_2	Total	Mg#	Rb	Sr	Ba	Cs	Sc	V	Cr	Co	Ni	Cu	Zn	Y
Lava and silicate portions of the breccia																											
TAF5 S	Cabezo negro de Tallante	47.13	2.62	16.26	9.38	0.14	6.22	7.93	3.48	2.71	0.77	3.79		100.43	0.61	68	868	808	2.6	15	194	180	31	150	30	90	20
TAF8 WR	Cabezo negro de Tallante	47.55	2.57	16.23	9.74	0.16	6.62	8.09	3.88	3.02	0.88	1.22		99.96	0.61	77	880	844	2.9	15	206	160	32	120	30	90	23
TAF12 S	Cabezo negro de Tallante	48.17	2.31	15.58	9.23	0.15	6.90	7.36	3.85	2.70	0.77	3.23		100.25	0.64	72	799	819	3.6	15	185	240	35	180	30	100	21
TAF17 WR	Cabezo negro de Tallante	45.45	3.01	16.50	10.48	0.16	5.56	8.36	3.26	3.08	0.89	2.70		99.45	0.55	80	987	1280	2.6	16	250	50	35	70	30	110	24
TAF23 WR	Cabezo negro de Tallante	47.81	2.49	15.09	9.81	0.15	6.61	8.59	4.30	1.07	0.84	1.87	0.08	98.63	0.61	18	839	822	2.9	15	209	190	37	160	40	100	20
TAF25 S	Cabezo negro de Tallante	48.64	2.25	13.60	9.22	0.14	8.55	7.21	3.10	2.15	0.55	2.80		98.20	0.68	63	736	781	3.1	14	173	370	37	310	30	90	16
TAF29 WR	Cerro Paalràn	46.69	2.72	15.32	10.31	0.17	6.51	9.99	4.87	1.46	0.90	1.48		100.42	0.60	15	950	968	2.9	18	258	190	36	120	40	100	22
TAF30 WR	Fuente vieja	47.47	2.51	15.22	9.58	0.15	5.64	9.08	4.26	1.10	0.81	2.36		98.19	0.58	74	895	922	3.3	15	215	200	36	140	40	110	21
TAF31 WR	Los Albadalejos	48.52	2.48	14.87	9.16	0.15	6.04	8.55	3.46	2.34	0.71	2.39		98.66	0.61	83	972	1728	3	15	211	190	32	130	30	100	19
TAF32 S	Los Albadalejos	47.58	2.52	15.04	9.04	0.15	5.91	8.69	3.24	2.41	0.63	3.46		98.66	0.60	72	984	4513	2.7	15	208	190	31	130	30	90	19
TAF34 WR	Los Puertos	50.40	2.12	15.35	9.16	0.15	5.75	8.00	3.69	2.31	0.82	0.62		98.37	0.59	55	808	853	2.4	15	199	190	33	140	30	90	20
TAF36 WR	Pico Cebolla	46.85	2.67	14.32	10.12	0.16	7.45	9.73	4.09	1.01	0.85	1.31		98.56	0.63	27	819	811	2.4	19	247	220	40	140	40	90	21
Breccia whole rock																											
TAF5 WR	Cabezo Negro de Tallante	36.51	1.86	11.86	7.40	0.12	5.46	18.00	2.32	1.56	0.68	13.27	9.33	99.04	0.63	51	784	534	2.4	10	135	140	24	120	20	60	16
TAF5 C	Cabezo Negro de Tallante	26.40	1.25	8.22	5.06	0.08	4.86	26.33	1.43	1.10	0.53	23.04	17.30	98.30	0.69	32	704	401	1.4	7	88	130	20	120	30	60	10
TAF12 WR	Cabezo Negro de Tallante	37.47	1.64	11.32	7.39	0.12	7.26	17.08	2.71	1.74	0.67	11.22	8.36	98.62	0.70	47	734	632	2.6	11	136	270	31	240	30	90	15
TAF25 WR	Cabezo Negro de Tallante	40.95	1.94	13.30	7.82	0.12	5.36	15.04	3.26	1.90	0.75	9.11	6.29	99.56	0.61	54	786	757	3.5	12	155	130	28	120	30	80	17
TAF27 WR	Casas de Tallante	28.02	1.44	8.45	5.55	0.09	3.89	27.50	1.17	1.05	0.66	21.87	16.70	99.69	0.62	28	659	524	1.9	9	132	100	19	60	30	60	12
TAF32 WR	Los Albadalejos	27.00	1.35	8.71	5.15	0.08	3.83	27.48	1.96	1.38	0.43	20.93	18.10	98.31	0.63	40	738	2069	1.5	8	111	100	16	70	20	60	11

Sample	Locality	SiO_2	TiO_2	Al_2O_3	Fe_2O_3	MnO	MgO	CaO	Na_2O	K_2O	P_2O_5	L.O.I	CO_2	Total	Mg#	Rb	Sr	Ba	Cs	Sc	V	Cr	Co	Ni	Cu	Zn	Y
TAF37 WR	Pico Cebolla	36.88	2.02	10.94	7.75	0.12	5.59	19.26	2.15	0.63	0.95	12.52	8.26	98.80	0.63	6	747	668	5.4	15	189	180	32	120	40	70	17
Calcrete																											
TAF1 WR	Cabezo Negro de Tallante	5.21	0.16	1.36	0.70	0.02	2.12	46.61	0.25	0.19	0.13	42.20	35.00	98.94	0.88	9	984	128	0.5	1	15		2	30	10		3
TAF28 WR	Casas de Tallante	9.17	0.37	2.81	1.54	0.03	1.19	45.41	0.26	0.30	0.14	38.12	33.50	99.35	0.64	12	443	139	0.8	3	35	30	5	20	10		5
TAF38 WR	Pico Cebolla	6.38	0.23	1.73	0.98	0.02	1.08	47.54	0.18	0.16	0.16	40.63	35.10	99.09	0.72	11	389	110	0.7	2	23	30	5	20	20		5
Carbonate fraction of breccia																											
TAF32 C	Los Albadalejos	2.69	0.08	0.72	0.32	0.01	1.14	50.10	0.23	0.05	0.03	43.05	39.70	98.41	0.89		567	152			7				10		2
Cumulate																											
TAF4 WR	Cabezo Negro de Tallante	46.66	1.62	7.24	9.69	0.15	16.86	16.30	1.13	0.33	0.15	0.16		100.29	0.80	5	208	152		44	264	1620	66	430	60	70	14
TAF11 WR	Cabezo Negro de Tallante	45.80	2.63	9.62	8.97	0.13	13.57	17.23	1.33	0.46	0.10	0.74		100.58	0.78	5	259	173		51	402	350	48	240	30	40	19
Schist																											
TAF26 WR	Cabezo Negro de Tallante	71.76	0.86	12.94	4.60	0.04	1.74	0.58	1.95	2.03	0.12	2.24		98.85	0.47	87	113	357	5.9	11	99	70	14	40	30	80	23

As expected, the breccia WR compositions are shifted towards much lower SiO_2 (26.4–40.9 wt%) and lower alkali (2.8–5.7 wt%) due to the dilution with the carbonate component (inset in Fig. 3; Electronic Appendix 6). The two cumulate samples are characterized by a relatively low SiO_2 (~45.8–46.7 wt%), coupled with very low alkali content ($Na_2O + K_2O$ = 1.5–1.8 wt%). Just for comparison, the schist is characterized by a high content of SiO_2 (71.76 wt%), with relatively low total alkalis (4.1 wt%).

A nearly perfect negative correlation of SiO_2 with CaO (R^2 = 0.995) can be observed in Fig. 4. Here, the WR breccias plot exactly in between the basaltic and the carbonate rocks (the calcrete and the carbonate fraction of the breccias). The TiO_2 content in all the basaltic samples range from ~2.1 to ~3.0 wt%, much higher than the other Betics and Malaga volcanic rocks (TiO_2 < 2 wt%). On the other hand, the same oxide reaches very low content in the carbonate samples (TiO_2 = 0.1–0.4 wt%). The WR breccias are characterized by intermediate contents (TiO_2 = ~1.2–2.0 wt%). The same features are repeated for all the other major oxides, with WR breccias always in between the basaltic compositions and the nearly pure carbonate lithologies (Fig. 4 and diagrams in Electronic Appendix 6).

For all the major oxides, the basaltic samples overlap the data from the Tallante-Cartagena literature (Electronic Appendix 6). The Mg/(Mg + Fe^{2+}) ratio, i.e. the Mg#, calculated using a Fe_2O_3/FeO ratio of 0.15, ranges from 0.55 to 0.68 in the basaltic rocks and from 0.61 to 0.70 in the WR breccias (Table 1). The CO_2 content has been measured in the WR breccias (6.3 to 18.1 wt%), the carbonate samples (33.5 to 39.7 wt%; Table 1) and in one basaltic rock sample (TAF23WR; CO_2 = 0.08 wt%). The mass Loss On Ignition, (labelled as L.O·I. in Table 1 and Electronic Appendix 6), reaches its greatest value in the carbonate samples. In TAF32C (carbonate fraction) L.O·I is 43.0 wt%, a value which includes also CO_2. The lowest values are in the lavas, with TAF34 having a L.O·I of 0.6 wt%. L.O.I in the whole rock analyses on the breccias have an intermediate value (from 9.1 to 21.9 wt%), with CO_2 accounting to ~66 to ~86% of L.O.I. (average ~ 74%).

6.2. Trace elements

Large Ion Lithophile Elements (LILE; Table 1; Fig. 5; details in Electronic Appendix 6) show a general negative trend vs. CaO, less evident for Rb because of the large compositional range for most basaltic rocks. Strontium is characterized by a negative trend too, but one calcrete-type carbonate sample (TAF1) falls out of the main pattern, being displaced towards relatively high Sr (984 ppm). Both the basaltic fraction (S) and the whole-rock composition (WR) of the breccia TAF32 are characterized by anomalously high Ba (5413 and 2069 ppm, respectively), partially disrupting the otherwise good negative correlation of this element with CaO. Also Cs shows a negative correlation with CaO, with the exception of one whole-rock breccia (TAF37WR). The ultramafic samples are out of the main trend, showing low LILE content, coherently with their cumulate nature.

Transition Elements (TE; Table 1; Fig. 5; details in Electronic Appendix 6) show an overall negative correlation with CaO for the entire database investigated. Some basaltic samples show a large spread in a relatively restricted CaO range, defining strong positive correlation with CaO (e.g., V vs. CaO R^2 = 0.73). In general, the cumulate rocks have higher TE content, up to four times the highest TE content of basaltic lavas (e.g., Cr up to 1620 ppm). The carbonate rocks continue to show nearly sterile compositions, while the whole-rock breccias plot in between the basaltic and the carbonate rock clusters.

High Field Strength Elements (HFSE; Table 1; Fig. 5; details in Electronic Appendix 6) are characterized by clear negative trends when plotted versus CaO, with R^2 > 0.94. Also in this case, basaltic rocks show the largest variation, similarly to what observed for Tallante volcanic rock literature data. The cumulate samples fall out of the main trend, being displaced towards low to very low HFSE content (e.g., Ta <1 ppm). The schist is particularly rich in Zr (289 ppm) and Hf (7.3 ppm) compared to basaltic rocks (maximum values 272 and 6.5 ppm for Zr and Hf, respectively). The analysed schist is characterized by peculiar low Nb (13 ppm) and Ta (1.1 ppm), much lower than those of the basaltic rocks (minimum values 66 and 4.8 ppm for Nb and Ta, respectively).

Light Rare Earth Elements (LREE; Table 1; Fig. 5; details in Electronic Appendix 6) trends vs. CaO exactly match what already observed for the other element groups, displaying clear negative correlations with R^2 ranging from 0.90 (Yb) to 0.95 (Ce). Specifically, the basaltic rocks show poor trends with CaO, generally characterized by low correlation coefficients (R^2 decreasing from ~0.44 to ~0.08 with increasing atomic number). The cumulates show lower REE abundances with respect to the main trend followed by the basaltic and carbonate samples. The LREE content of the schist is sensibly lower than that of the basaltic rocks (e.g., ~30 vs. ~45–68 ppm), but progressively becomes more abundant in the HREE (Heavy REE; e.g., Lu ~0.4 ppm for the schist; ~0.2–0.4 ppm for the basaltic rocks).

U-Th-Pb (Table 1; Fig. 5; details in Electronic Appendix 6) are characterized by negative correlations with CaO, with all the carbonate rocks showing Pb <5 ppm, i.e., below the ICP-MS detection limit. Exactly the same features observed in the previous groups can be identified here, with the overall major negative correlation (e.g., R^2 = 0.93 for U), a large spread of compositions in the basaltic rocks (e.g., Pb = 4–18 ppm; Th = 14–22 ppm) and low content in the cumulate rocks (e.g., Pb ~5 ppm; Th ~2–6 ppm; U = 0.4–1.1 ppm).

6.3. Primitive mantle- and CI chondrite-normalised diagrams

Primitive mantle-normalised multielemental diagrams for the basaltic rocks, WR breccias and carbonate components, together with those of the basement schist and the two cumulate rocks, are reported in Fig. 6 (all the diagrams can be found in Electronic Appendix 6). Except for some trough at Rb and, less evident, at Ba, the trend defined by the basaltic rocks is very smooth with only small troughs and peaks (Fig. 6a). Nearly all the elements plot along a rather straight line, with four over twelve samples showing negative K anomalies, and all the samples showing small troughs at Sm and Y as well. The carbonate samples share overall the same gross features of the basaltic rocks, but they are displaced towards lower incompatible element content. They also show slightly spikier patterns, with negative anomalies at Rb, Ba, K and Ti, coupled with strong peaks at Sr and U (Fig. 6b). Interestingly, the higher the CaO the lower the absolute incompatible element content, with sample TAF32C (calcrete; CaO = 50.1 wt%) being characterized by the lowest incompatible element content (Fig. 6b). Whole-rock composition of the breccias plots in between the basaltic and carbonate rocks (Fig. 6b), but much closer to the first ones. Overall, the same interelemental fractionation observed for the basaltic rocks emerges for WR breccias.

The two cumulate rocks show overall similar intra-elemental fractionation, displaced towards lower absolute incompatible element concentrations compared to the basaltic rocks and a generally flatter pattern (Fig. 6c). The only relevant characteristic is the slight negative anomaly at P and Zr. The schist shows a spikier pattern, with strongly incompatible elements generally lower than the basaltic rocks, but with the least incompatible elements roughly overlapping those of the basaltic rocks (Fig. 6c).

The CI chondrite-normalised REE pattern of the basaltic rocks (Fig. 7a; all the diagrams reported in Electronic Appendix 6) is straight, with moderate fractionation [$(La/Lu)_N$ ~ 18–25], no relevant Eu/Eu* anomalies (0.95–1.09) and quite flat HREE [$(Ho/Lu)_N$ ~ 1.2–1.6]. Carbonate rocks (Fig. 7b) are displaced towards much lower REE and lower

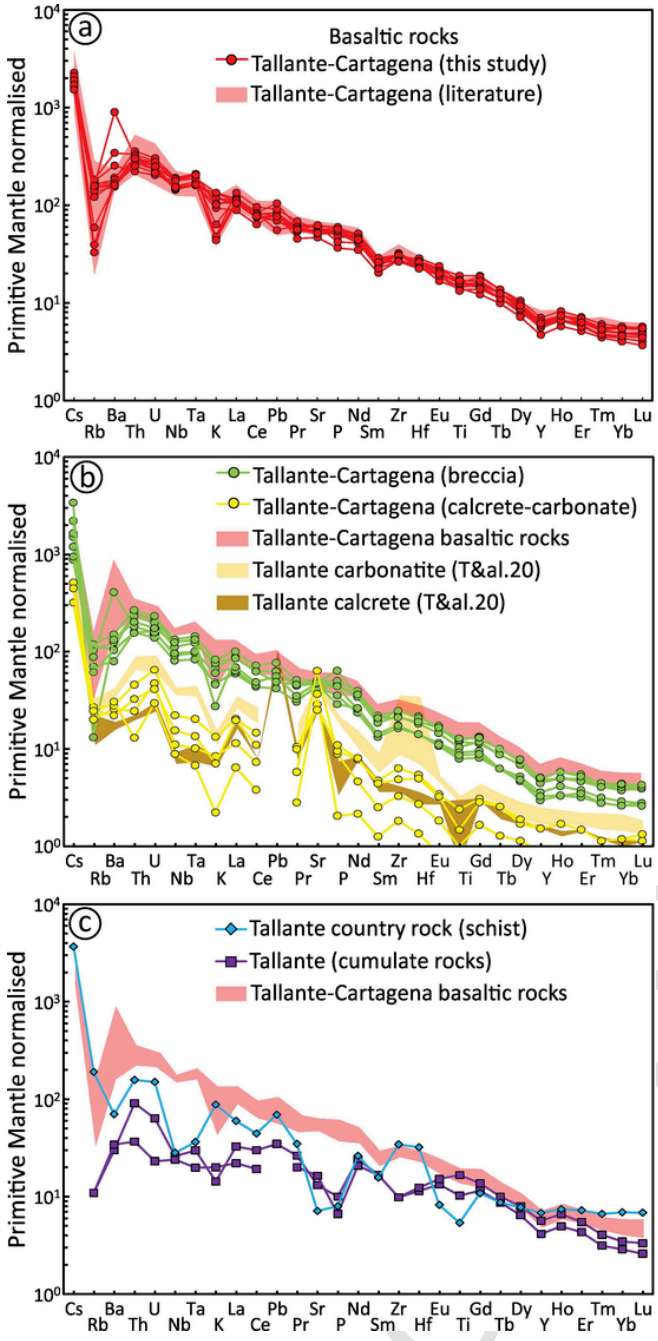

Fig. 6. Primitive mantle-normalised (normalizing factors after Lyubetskaya and Korenaga, 2007) incompatible element patterns for Tallante rocks investigated in this study. (a) Basaltic samples. The grey field represent the literature data for the area of Tallante and Cartagena (Beccaluva et al., 2004; Capedri et al., 1989; Cebriá et al., 2009; Duggen et al., 2005; Turner et al., 1999). (b) Breccia whole-rock and carbonate samples. The grey field report the values from the basaltic rocks from this study. The data of the carbonate fraction of Toscani et al. (2020) are also plotted as a yellow field. (c) Cumulate and schist samples. (For interpretation of the references to colour in this figure legend, the reader is referred to the web version of this article.)

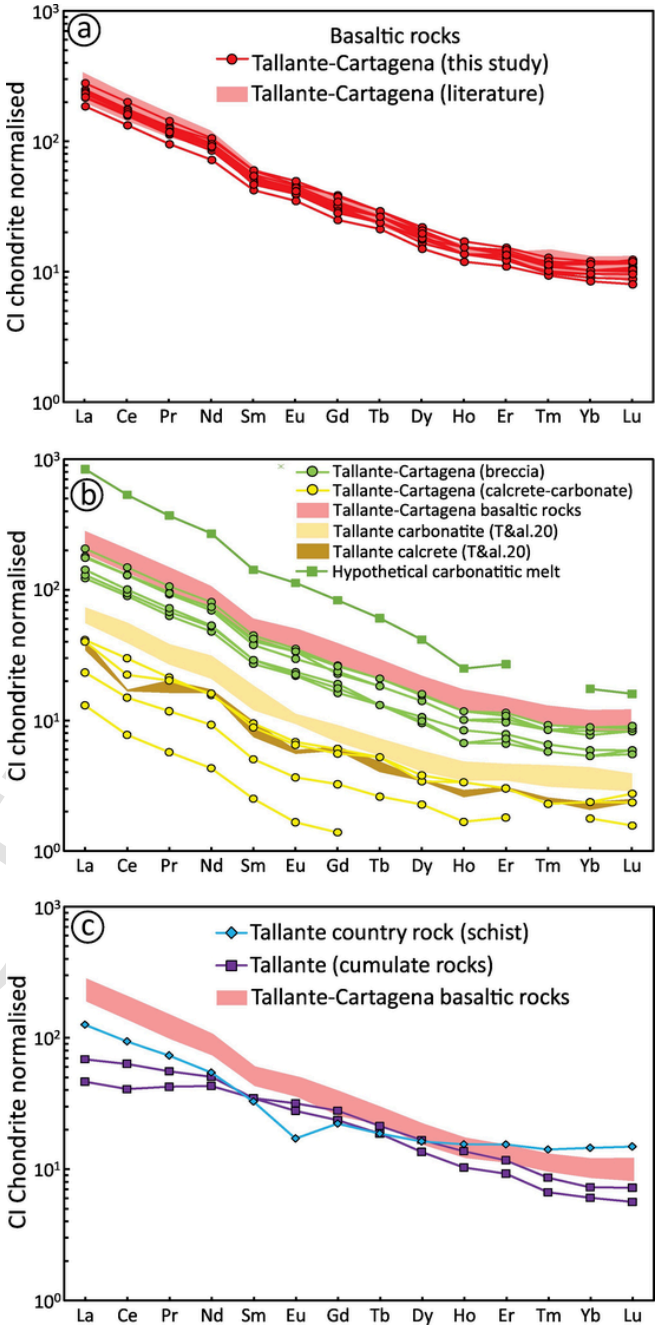

Fig. 7. CI Chondrite-normalised (normalizing factors after King et al., 2020) REE patterns for Tallante rocks investigated in this study. (a) Basaltic samples. The grey field represent the literature data for the area of Tallante and Cartagena (Beccaluva et al., 2004; Capedri et al., 1989; Cebriá et al., 2009; Duggen et al., 2005; Turner et al., 1999). (b) Breccia whole-rock and carbonate samples. The grey field report the values from the basaltic rocks from this study. The data of the carbonate fraction of Toscani et al. (2020) are also plotted as a yellow field. The hypothetical REE pattern of a carbonatite in equilibrium with the basaltic sample with the highest MgO content, calculated with the empirical correlation proposed by Nabyl et al. (2020) is also shown. (c) Cumulate and schist samples. (For interpretation of the references to colour in this figure legend, the reader is referred to the web version of this article.)

LREE/HREE fractionation [$(La/Lu)_N \sim 15–17$], slight Eu/Eu* negative anomaly (0.88–0.91) and flat HREE [$(Ho/Lu)_N \sim 1.1–1.5$]. WR breccias (Fig. 7b) plot in between the basaltic and carbonate rock compositions, with similar inter-REE fractionation patterns. Fig. 7b also shows the REE pattern for a hypothetical carbonatitic rock, formed by a melt in equilibrium with the composition of the basaltic sample characterized by the highest content of MgO (TAF25S), as calculated with the model proposed by Nabyl et al. (2020). Details on this aspect are reported in the discussion section. The two cumulate rocks have lower LREE/HREE fractionated compositions [$(La/Lu)_N \sim 6.4–12.2$], no Eu/Eu* anomalies (0.96–1.01), nearly flat HREE [$(Ho/Lu)_N \sim 1.9–2.0$] and slightly convex upward pattern (Fig. 7c). The schist shows flatter pattern [$(La/Lu)_N \sim 8.5$], a clear Eu/Eu* negative anomaly (0.63) and a completely flat HREE trend [$(Ho/Lu)_N \sim 1.1$; Fig. 7c].

7. Isotope geochemistry

7.1. Radiogenic isotopes

The Rb—Sr, Sm—Nd, U-Th-Pb isotopic systematics have been analysed on eight representative samples: two silicate fractions of the breccias (TAF25S and TAF32S), two whole-rock breccias (TAF25WR and TAF32WR), two carbonate rocks (a calcrete, TAF28WR, and a carbonate fraction of a breccia, TAF32C), and one schist (TAF26). Results are reported in Table 2. We only report the measured Sr-Nd-Pb isotopic values because of the young age of the rocks. All the data, including those from literature, are reported in Electronic Appendix 6.

The measured $^{87}Sr/^{86}Sr$ isotope ratios are higher than the present-day BSE (0.70445) for all the analysed samples. Both the basaltic fraction of the breccias and the basaltic lava flow rocks have $^{87}Sr/^{86}Sr$ ratios slightly above this value (0.70451–0.70452; Fig. 8a), well within the literature field for Tallante basaltic rocks (0.70375–0.70456; Capedri et al., 1989; Turner et al., 1999; Beccaluva et al., 2004; Duggen et al., 2005; Cebriá et al., 2009). The WR breccias are displaced towards more radiogenic $^{87}Sr/^{86}Sr$ isotope ratios (0.70493–0.70555). The calcrete sample (TAF28WR) shows higher $^{87}Sr/^{86}Sr$ (0.70715), and an even higher value is are found for the carbonate fraction of sample TAF32C ($^{87}Sr/^{86}Sr$ = 0.70800). The $^{87}Sr/^{86}Sr$ isotope ratio for the cumulate sample (0.70538) is sensibly higher than the BSE value. The $^{87}Sr/^{86}Sr$ isotope ratios show good correlations with CaO and SiO_2 (R^2 = 0.97 for both parameters; Fig. 8b and c). The schist is characterized by the highest $^{87}Sr/^{86}Sr$ (~0.71881), consistent with the fact that it represents an ancient (likely related to Variscan/Hercynian Orogeny) upper continental crust fragment with relatively high Rb/Sr (0.77).

With the exception of the schist sample, the analysed rocks show a range of $^{143}Nd/^{144}Nd$ from 0.512450 to 0.512751, straddling the ChUR estimate (Chondritic Uniform Reservoir = 0.512638). The schist again plots in a very different position ($^{143}Nd/^{144}Nd$ = 0.51200; Fig. 8a), due to the retarded radiogenic growth of ^{143}Nd caused by the low Sm/Nd ratio (0.20). The basaltic rocks have $^{143}Nd/^{144}Nd$ ratios higher than ChUR (0.512695–0.512744), the carbonate fraction is less radiogenic (0.512450–512,552), and the whole-rock breccia plot in between this range (0.512647–0.512751).

The $^{206}Pb/^{204}Pb$ isotopic ratios decrease from the values of the basaltic rocks (18.90–18.91) to those of carbonates (18.44–18.63). The breccias show intermediate ratios (18.83–18.87). A good correlation of $^{206}Pb/^{204}Pb$ with SiO_2 (R^2 = 0.89) and a negative correlation with CaO (R^2 = 0.89) can be observed (Electronic Appendix 6). $^{206}Pb/^{204}Pb$ correlates almost perfectly vs. $^{87}Sr/^{86}Sr$ (R^2 = 0.97; Fig. 8d) and less clearly vs. $^{143}Nd/^{144}Nd$ (R^2 = 0.57; Fig. 8e; Electronic Appendix 6). The $^{207}Pb/^{204}Pb$ almost coincides for breccias and lavas (15.66–15.67 and 15.66–15.68, respectively), while the carbonate portion shows slightly lower ratios (15.65–15.62). $^{208}Pb/^{204}Pb$ ranges between 39.01 and 39.04 for basaltic rocks, between 38.94 and 39.01 for breccias and between 38.46 and 38.68 for the carbonate fraction. Fig. 8f shows the excellent negative correlation between $^{207}Pb/^{206}Pb$ and $^{208}Pb/^{206}Pb$ (R^2 = 0.99). The schist sample plots out of the main trend with $^{206}Pb/^{204}Pb \sim 18.76$, $^{207}Pb/^{204}Pb \sim 15.66$ and $^{208}Pb/^{204}Pb \sim 38.92$, while the only analysed cumulate rock has a $^{206}Pb/^{204}Pb \sim 18.84$, $^{207}Pb/^{204}Pb \sim 15.67$ and $^{208}Pb/^{204}Pb \sim 38.04$.

7.2. Stable isotopes

Oxygen and carbon isotopic compositions, reported as $\delta^{18}O_{SMOW}$, $\delta^{18}O_{PDB}$ and $\delta^{13}C_{PDB}$ in Table 2, have been analysed for three calcretes (TAF1WR, TAF28WR and TAF38WR) and for five carbonate fractions of the pyroclastic breccias (TAF12C, TAF25C, TAF27C, TAF32C and TAF35C). The $\delta^{18}O_{SMOW}$ values are quite heavy and vary in a relatively restricted range (from +25.5 to +28.3‰). They mostly fall within the oxygen isotopic range measured by Toscani et al. (2020) for the same rock types ($\delta^{18}O_{SMOW}$ from +25.3 to +27.0‰). The $\delta^{13}C_{PDB}$ values are quite light and vary from −5.9 to −9.9‰. Also in this case, the analyses mostly fall in the field measured by Toscani et al. (2020); from −4.8 to −10.3‰; Fig. 8h). These isotopic values fall in the O—C isotopic range of NE Spain Cenozoic calcretes (Alonso-Zarza and Arenas, 2004), i.e., $\delta^{18}O_{SMOW}$ from +23.4 to +27.4‰ and $\delta^{13}C_{PDB}$ from −4.2 to −8.2‰.

The $\delta^{13}C_{PDB}$ and $\delta^{18}O_{SMOW}$ of the Tallante carbonate fraction is compared with the fields of the primary carbonatites (Taylor Jr et al., 1967), marine limestones (Grossman, 2012) and calcrete/dolocrete (Alonso-Zarza et al., 2020; Alonso-Zarza and Arenas, 2004) in Fig. 8h. Tallante carbonates are displaced towards much heavier $\delta^{18}O_{SMOW}$ compared to primary carbonatites and much lighter $\delta^{13}C_{PDB}$ compared with marine limestones, but show a rough overlap with calcrete and dolocrete crusts.

8. Discussion

The main goal of this study is the comprehension of the nature and the origin of the whitish carbonate-rich matrix that agglutinates the basaltic fragments in the pyroclastic breccia found in Cabezo Negro de Tallante and in the neighbouring igneous outcrops (Cerro Palaràn, Pico Cebolla, Fuente vieja, Los Albadalejos and Los Puertos). The secondary aim of this study is to constrain the conditions that led to the generation of basaltic melts in the Tallante-Cartagena area.

8.1. Carbonatite or carbonate?

Associations between carbonate-rich and silicate magmas are well known in literature (Woolley and Bailey, 2012; Woolley and Kjarsgaard, 2008), albeit it is not always easy to distinguish between the sedimentary carbonate and carbonatitic components. For example, carbonate-rich lithologies in central Italy classically interpreted in literature as true carbonatites (e.g., Stoppa et al., 2005) have been instead classified as pseudocarbonatites (e.g., Lustrino et al., 2019) or mixed ultrabasic melts generated after the digestion of marly upper crustal lithologies by ultrabasic compositions (e.g., Lustrino et al., 2020; Peccerillo, 2004). In other cases, some carbonate-rich rocks in S India, classified as sövite (i.e., coarse-grained Ca-carbonatite) and alvikite (i.e., fine-grained Ca-carbonatite) decimetre-thick dykes (Santosh et al., 1987) have been reinterpreted as granulite-facies metacarbonates with sedimentary protoliths (e.g., Hegner et al., 2020).

The pyroclastic breccia of Tallante offers an interesting opportunity to investigate in detail this diatribe. Toscani et al. (2020) focused their study on the whitish carbonate component of the polymictic breccia lying below the main lava flow at Cabezo Negro de Tallante volcano. These authors interpreted the compositional variability of the carbonate matrix (CaO = 34.6–27.7 wt%; CO_2 = 24.8–30.8 wt%; SiO_2 = 13.8–17.0 wt%; Al_2O_3 = 3.79–4.79 wt%; MgO = 2.94–4.30 wt%; $Na_2O + K_2O$ = 0.7–1.1 wt%) as related to the presence of variable amounts of tiny silicate rock fragments in a carbonatitic matrix. Toscani et al. (2020) used the particularly heavy $\delta^{18}O$ and the light $\delta^{13}C$ values of the carbonate component to confirm an igneous origin, despite they represent the typical caliche-calcrete compositions (Alonso-Zarza et al., 2020; Alonso-Zarza and Arenas, 2004). The incompatible element contents of the Cabezo Negro de Tallante carbonate fraction are much lower than the average compositions of Ca-carbonatites (Chakhmouradian, 2006; Woolley and Kempe, 1989), rendering at least improbable any connection with true Ca-carbonatitic melts.

Table 2
$^{87}Sr/^{86}Sr$, $^{143}Nd/^{144}Nd$, $^{206}Pb/^{204}Pb$, $^{207}Pb/^{204}Pb$, $^{208}Pb/^{204}Pb$, $\delta^{18}O_{(SMOW)}$, $\delta^{18}O_{(PDB)}$ and $\delta^{13}C_{(PDB)}$ isotopic ratios of Tallante area volcanic, sedimentary and metamorphic rocks.

Sample	Locality	$^{87}Sr/^{86}Sr$	±	$^{143}Nd/^{144}Nd$	±	$^{206}Pb/^{204}Pb$	±	$^{207}Pb/^{204}Pb$	±	$^{208}Pb/^{204}Pb$	±	$^{208}Pb/^{206}Pb$	$^{207}Pb/^{206}Pb$	Δ7/4	Δ8/4	$\delta^{18}O_{(smow)}$	±	$\delta^{18}O$
Lava and silicate portions of the breccia																		
TAF25S	Cabezo negro de Tallante	0.704521	0.000004	0.5126950	0.000005	18.90	0.0013	15.68	0.0012	39.04	0.0029	2.07	0.83	14.0	56.7			
TAF32S	Los Albadalejos	0.704508	0.000006	0.5127440	0.000002	18.91	0.0020	15.66	0.0016	39.01	0.0040	2.06	0.83	12.3	51.3			
Breccia whole rock																		
TAF25WR	Cabezo negro de Tallante	0.704934	0.000005	0.5126473	0.000012	18.87	0.0012	15.67	0.0010	39.01	0.0025	2.07	0.83	13.2	56.4			
TAF32WR	Los Albadalejos	0.705546	0.000005	0.5126473	0.000003	18.83	0.0020	15.66	0.0016	38.94	0.0040	2.07	0.83	12.6	54.2			
Calcrete																		
TAF1WR	Cabezo negro de Tallante															26.6	0.25	-4.2
TAF28WR	Casas de Tallante	0.707149	0.000009	0.5124500	0.000017	18.63	0.0018	15.65	0.0015	38.68	0.0039	2.08	0.84	13.6	52.6	27.9	0.25	-2.9
TAF38WR	Pico Cebolla															28.3	0.25	-2.5
Carbonate fraction of the breccia																		
TAF12C	Cabezo negro de Tallante															27.3	0.25	-3.5
TAF25C	Cabezo negro de Tallante															25.5	0.25	-5.2
TAF27C	Casas de Tallante															27.7	0.25	-3.1
TAF32C	Los Albadalejos	0.708004	0.000006	0.5125520	0.000008	18.44	0.0019	15.62	0.0014	38.46	0.0034	2.09	0.85	12.7	54.2	27.9	0.25	-2.9
TAF35C	Los Puertos															25.7	0.25	-5.1
Cumulate																		
TAF4WR	Cabezo negro de Tallante	0.705382	0.000006	0.5125680	0.000002	18.84	0.0015	15.67	0.0011	39.04	0.0033	2.07	0.83	13.6	63.0			
Schist																		
TAF26WR	Cabezo negro de Tallante	0.718816	0.000005	0.5120059	0.000013	18.76	0.0008	15.66	0.0007	38.92	0.0014	2.07	0.83	13.7	60.7			

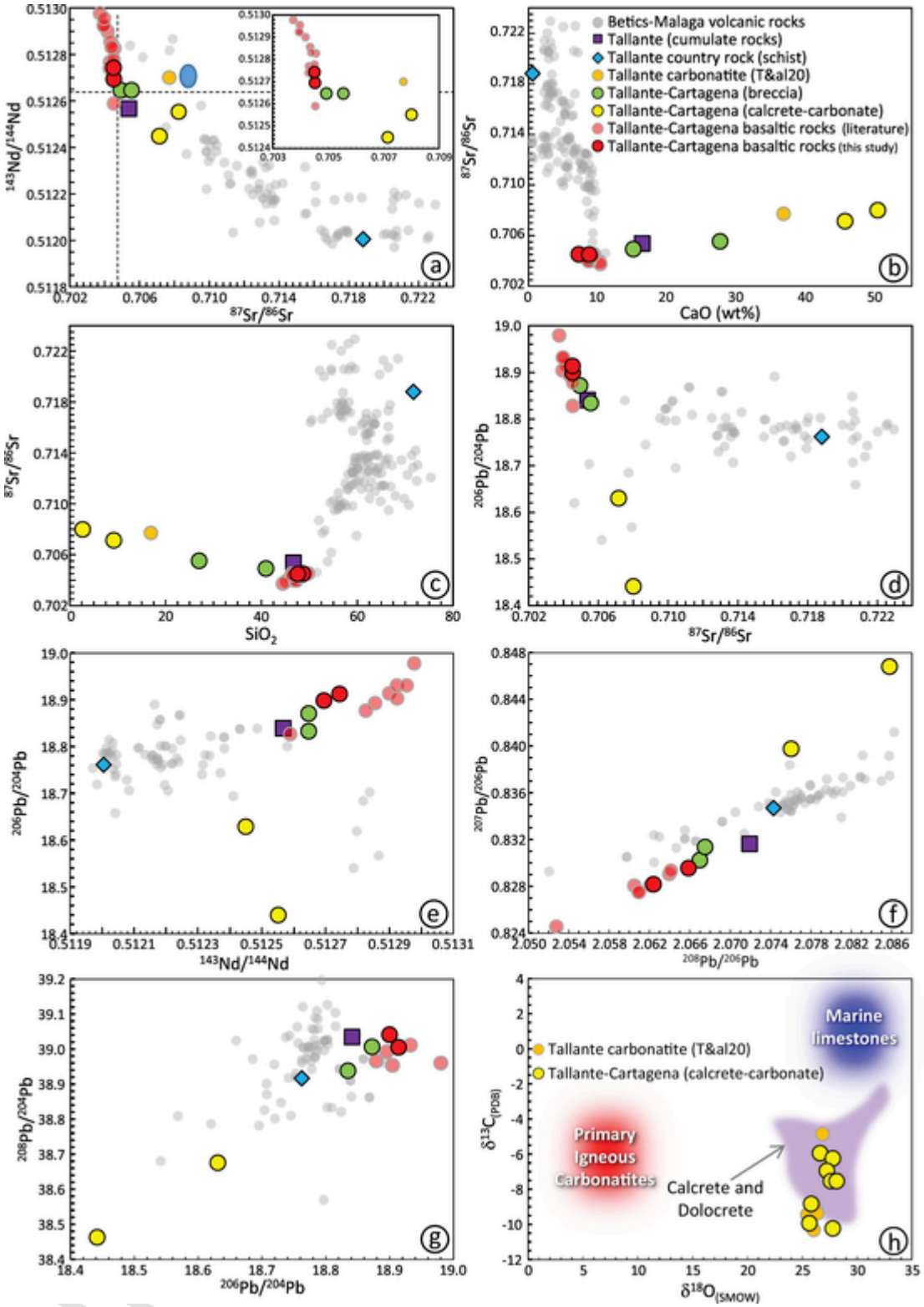

Fig. 8. (a) $^{143}Nd/^{144}Nd$ vs. $^{87}Sr/^{86}Sr$ diagram. (b) $^{87}Sr/^{86}Sr$ vs. CaO diagram. (c) $^{87}Sr/^{86}Sr$ vs. SiO_2 diagram. (d) $^{206}Pb/^{204}Pb$ vs. $^{87}Sr/^{86}Sr$ diagram. (e) $^{206}Pb/^{204}Pb$ vs. $^{143}Nd/^{144}Nd$ diagram. (f) $^{207}Pb/^{206}Pb$ vs. $^{208}Pb/^{206}Pb$ diagram. (g) $^{208}Pb/^{204}Pb$ vs. $^{206}Pb/^{204}Pb$ diagram for Tallante rocks investigated in this study. References for Tallante-Cartagena basaltic rocks, for Betic-Malaga volcanic rocks and for Toscani et al. (2020) carbonates are reported in the caption of Fig. 3. (h) $\delta^{13}C_{(PDB)}$ vs. $\delta^{18}O_{(SMOW)}$ for the carbonate fraction of the breccia and the calcrete of Tallante area. The fields of primary igneous carbonatite (Taylor Jr et al., 1967), marine limestone (Grossman, 2012) and literature calcrete and dolocrete (Alonso-Zarza et al., 2020; Alonso-Zarza and Arenas, 2004) is reported for comparison.

8.2. Carbonatite-silicate melt pairs in the mantle

Schmidt and Weidendorfer (2018) emphasized that only strongly alkaline ultrabasic parental liquids ($Na_2O + K_2O \sim 3–7$ wt% and $SiO_2 \sim 37–40$ wt%) can drive the evolving melts into the silicate-carbonatite miscibility gap after prolonged fractional crystallization (Fig. 3). Entering the miscibility gap means the separation of two distinct melts from a single parental CO_2-rich silicate liquid with ultrabasic to intermediate composition (e.g., Brooker, 1998; Brooker and Kjarsgaard, 2011). The hawaiitic-basanitic composition of Cabezo Negro de Tallante and neighbouring basaltic rocks is far away from the composition where immiscibility can develop (Fig. 3). Despite this, Toscani et al. (2020) proposed the existence of an exsolution or immiscibility process that separates the carbonatitic component from the basaltic melt in a form of emulsion. We interpret the petrographic features shown by the authors (e.g., their Fig. 4B, D, F) as secondary calcite, filling vesicles in volcanic scoria, rather than the evidence of the immiscibility of carbonate droplets in a basaltic magma.

To reinforce our conclusion, we have plotted the compositions of the basaltic, carbonate and mixed rocks in the triangular plot Na_2O-($SiO_2 + Al_2O_3$)-CaO (Fig. 9), with the experimentally determined solvi between silicate and carbonatitic melts at variable P (0.2–2.5 GPa) and T (1125–1550 °C; Brooker and Kjarsgaard, 2011). The Tallante basaltic rocks plot distant from all the experimental solvi, being characterized by too low alkali content (Na_2O) and too high SiO_2 (Fig. 9). Also the carbonate component of Tallante-Cartagena (nearly alkali-free) is very different from the experimentally exsolved carbonatitic melts as determined by Brooker and Kjarsgaard (2011); grey dashed lines in Fig. 9a). The addition of H_2O, K_2O, TiO_2, MgO and FeO to the system does not change the shape of the solvi (Kjarsgaard, 1998; Martin et al., 2013).

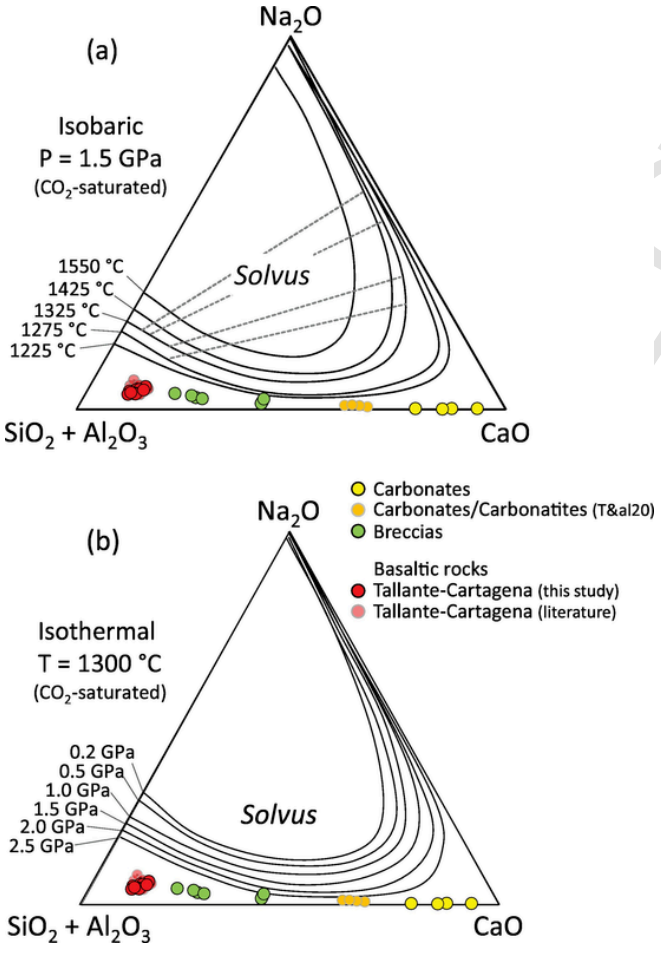

Fig. 9. Triangular plot ($SiO_2 + Al_2O_3$)-Na_2O-CaO for Tallante rocks investigated in this study. (a) Basaltic samples. The experimentally determined solvi between silicate and carbonatite melts at variable T (from 1125 to 1550 °C) and variable P (from 0.2 to 2.5 GPa) are reported (Brooker and Kjarsgaard, 2011). (a) Isobaric condition ($P = 1.5$ GPa). (b) Isothermal condition ($T = 1300$ °C).

In conclusion, our interpretation is compatible with the evidence that the composition of the basaltic rocks cannot lead to any silicate-carbonate immiscibility. Moreover, the carbonate portion associated to the basaltic rocks is certainly unrelated to any magmatic stage process, but reflects the interaction with a sedimentary component.

8.3. Petrographic evidence and mineral chemistry constraints

This study proposes a model involving pedogenic and ground water processes developed in a sub-aerial and continental environment. The presence of structures such as peloids, coated grains (Figs. 1e-f, 3c-f of Electronic Appendix 3), and alveolar septal structures in the carbonate fraction of Cabezo Negro pyroclastic breccias points to an intense microbial activity and root growth. The microbial activity can, indeed, lead to the typical clotted fabric (Figs. 1e-h, 3e-h of Electronic Appendix 3), but also to the development of concentric and wavy layers in the carbonate, effectively observed in thin sections (Figs. 1a-b, 3g and h of Electronic Appendix 3). Coated grains commonly occur in biogenic calcretes, due to the precipitation of concentric millimetric laminae of calcium carbonate, induced by the root activity (Alonso-Zarza and Wright, 2010).

Therefore, the features defined as carbonate micro-lapilli by Toscani et al. (2020) are here interpreted as peloids and pisoids. In our view, the composite lapilli are micrite with a clotted fabric. Indeed, roots favour the precipitation of carbonate by creating an alkaline environment but also by developing an optimal habitat for fungi and bacteria, which participate at the precipitation process (Wright and Tucker, 1991). The same effects can be associated to evaporation processes around pre-existing cores, i.e. former grains such as silicate scoriae (Fig. 3e and f of Electronic Appendix 3). This conclusion is strengthened by the finding of rhizoliths, with their typical *microcodium* features, septa and vacuoles (Figs. 1c, d, 3i and l of Electronic Appendix 3). The *microcodium* testifies the substitution of the cells by calcite crystals after the death of the plants. It is a common feature in paleo-soils, as well as the alveolar structures, led by the cementation of the former structures (Alonso-Zarza and Wright, 2010). Rhizoliths, peloids and pisoids clearly provide another clue about the continental environment where the carbonate was formed.

The mineral chemistry analyses carried out on these structures (peloids, coated grains, laminated matrix) clearly outline the sedimentary origin of the carbonate. All the carbonate nodules (core and rim), the carbonate matrix, the carbonate laminae, the carbonate filling of vesicles and the carbonate rims around volcanic scoriae chemically corresponds to Mg-poor calcite (maximum MgO = 2.99 wt%) with very low Fe (<0.26 wt%), Ba (<0.07 wt%) and Sr contents (<0.23 wt%). These trace element values fit perfectly the range of soil carbonates (e.g., Wright and Tucker, 1991). The only difference found among the carbonate portion is in the laminated carbonate around and in the scoria of TAF6, where compositions approaching that of dolomite are recorded (MgO = 19.2 wt%).

All these characteristics indicate that the Ca-rich portion of the breccia can be defined as calcrete and, more exactly, as biogenic or β-calcrete (sensu Wright, 1991). Consequentially, the origin of Cabezo Negro breccia can be related to interaction of basaltic rocks with the vadose zone and more specifically to the laminar portion of the pedogenic profile (e.g., Alonso-Zarza et al., 1998). The development of this paleosol was probably allowed by the alternation between dissolu-

tion and precipitation phases, with the predominance of an arid or semi-arid climate, coherently with what reported in literature (García, 1988; Geiger, 1970; Rosello Verger, 1970). An intense microbial, fungal and root activity is hypothesized, with a strong involvement of meteoric water too. This meteoric water was probably enriched in $CaCO_3$, because of a previous severe runoff and leaching phase or because it became enriched after its percolation into the ground, probably through older layers of carbonate, and then the evaporation brought to the rising and precipitation.

Indication on the sources of Ca can be achieved by the Sr isotope ratio of calcrete (Alonso-Zarza and Wright, 2010; Hamidi et al., 2001). This ratio may be controlled by different factors such as weathering of parent-rocks, input of surrounding calcareous formations, marine spray or rain and aeolian dust (Alonso-Zarza et al., 2020; Chiquet et al., 1999). The strontium isotope ratios clearly differ from those of the investigated volcanic rocks, while a contribution by surface water or groundwater cannot be excluded. The hydrogeology setting of the Campo de Cartagena evidence that the main aquifers are constituted by limestone, sand and conglomerate of Tortonian to Messinian age, and sandstone of Pliocene age. The Tortonian limestone has Sr isotope ratio ranging between 0.708945 and 0.708836. However, a contribution of Sr isotopes and Ca of the calcrete may also be derived from weathering of Middle-Upper Triassic carbonates outcropping in the nearby Sierra del Algarrobo. The Middle-Upper Triassic carbonates show Sr isotope ratios ranging between 0.70760 and 0.70790. This last source likely dominates the Sr isotope fingerprint of the calcrete analysed in this study.

8.4. Presence of dolomite and dolocrete

Toscani et al. (2020) considered the presence of dolomite at Tallante as the key feature to infer a mantle origin for the carbonate fraction. These authors proposed an original dolomitic melt transformed into calcite + periclase + CO_2, with the vapour phase acting as the propellant for the explosive activity. Toscani et al. (2020) explained the complete absence of periclase in the Cabezo Negro de Tallante volcano assuming the persistence of MgO in the silicatic melt fraction. The basaltic melt enriched by MgO related to the dolomite break-down would then enhance olivine crystallization from the silicate fraction of the magma.

Worth noting, dolomite is a common phase in many sediments and regoliths indurated by eodiagenetic cements, common in many sub-humid to arid landscapes, defined as dolocretes (Alonso-Zarza and Wright, 2010; Bustillo and Alonso-Zarza, 2007; Mather et al., 2019; Wright and Tucker, 1991). Dolomite can crystallize both as replacement of a carbonate precursor (dolomitization) or by direct precipitation (primary nucleation) in lacustrine, saline-evaporitic and phreatic environments (e.g., Mather et al., 2019). Consequentially, the presence of dolomite cannot be considered as a proof to infer a clear mantle-derived origin for the carbonate component at Tallante.

8.5. Geochemical and isotopic constrains

Major and trace element compositions of the carbonate fraction of the breccia samples analysed in this study are indistinguishable from those of the calcrete crusts (Table 1; Figs. 4 and 5). TAF32C, the carbonate fraction mechanically separated from a breccia, with the lowest incompatible element content, has low LILE (Rb <2 ppm, Sr = 567 ppm; Ba = 152 ppm), very different from the average Ca-carbonatite composition (Rb = 14 ppm; Sr = 7272 ppm; Ba = 3044 ppm; Woolley and Kempe, 1989; Chakhmouradian, 2006). Also the HFSE contents of TAF32C sample (Zr = 15 ppm; Nb = 4 ppm; Hf = 0.3 ppm; Ta = 0.2 ppm) are much lower than the average Ca-carbonatite composition (Zr = 281 ppm; Nb = 343 ppm; Hf = 9.1 ppm; Ta = 4.9 ppm). The difference in terms of REE (ΣREE = 11.87 ppm for TAF32C vs. 3731 ppm for average Ca-carbonatites) is even stronger. The trends of the major oxides and trace elements vs. CaO clearly show an enrichment for the basaltic rocks, while the carbonate portion is always characterized by the lowest content, and the mixed composition plotting always on the mechanical mixing line between these two extremes. The compositional variability of the WR breccias depends on the proportion of basaltic fragments in the carbonate matrix, as well as the different evolution degree of the various basaltic batches.

The most evolved basaltic sample (TAF17; 5.56 wt% MgO) is mixed with a hypothetically pure limestone, without any other major oxide content. This modelling mimics a mechanical interaction between a basaltic component with either poorly consolidated carbonate sediments or the simple mechanical mixing between two solid sources. Fig. 4 shows also a second mechanical mixing line starting from the least evolved basaltic sample (TAF25S; 8.48 wt% MgO) mixed with an "impure" marly carbonate composition, assumed to have SiO_2 = 3.0 wt%, TiO_2 = 0.0 wt%, Al_2O_3 = 0.5 wt%, Fe_2O_3 = 0.2 wt%, MnO = 0.0 wt%, MgO = 2.0 wt%, CaO = 50.0 wt%, Na_2O = 0.1 wt%, K_2O = 0.1 wt%, P_2O_5 = 0.05 wt%. The whole-rock breccia compositions plot always along the mixing lines (Fig. 4), with basalt/carbonate ratios between 90/10 and 50/50. The absence of typical skarn minerals, as well as the absence of CaO-rich olivine rims, monticellite-kirchsteinite solid solution, melilite or other mineral paragenesis typical of digestion of limestone by a basic-ultrabasic magma (see discussion in Lustrino et al., 2020), are features compatible with interaction in conditions close to those occurring at Earth's surface.

Radiogenic and stable isotopes reveal unambiguous distinct sources for silicatic and carbonatic components (Fig. 8). The extreme correlation between several isotopic ratios with major oxides (e.g., Fig. 8; Electronic Appendix 6) indicate: a) a mantle origin for the basaltic compositions; b) the impossible derivation of the carbonate fraction from the same mantle source that generated the basaltic rocks; c) the strong crustal origin for the carbonate component, linked to low-T water circulation.

8.6. Inferences on the degree of melting and mantle mineralogy

To infer the degree of melting and the amount of spinel and/or garnet in the source of the basaltic rocks, a first attempt has been made assuming as mantle source composition the lithospheric mantle average estimate of McDonough (1990). Fig. 10a reports Gd/Lu vs. La diagram aiming to infer the degree of melting and the spinel/garnet ratio. The assumed ol:opx:cpx:sp./gt modal ratio has been set to 55:30:12:3 to calculate D (bulk partition coefficient), while the same mineral ratios entering the melts (parameter P in Shaw, 1970) has been assumed to be −22:38:71:13. Olivine appears with a negative value due to the incongruent melting of orthopyroxene, which leads to an increase of modal olivine in the residual mantle (e.g., Baker and Stolper, 1994). The partition coefficient used are taken from the GERM database (http://earthref.org/GERM/), and are reported in the Electronic Appendix 6, with the references. In the Gd/Lu vs. La diagram (Fig. 10a), the composition of the hypothetical melts produced at different degrees of melting and with a spinel/(spinel+garnet) ratio ranging from 0 (only garnet) to 1 (only spinel) are reported and compared with the actual composition of the basaltic rocks. The presence of fractional crystallization processes certainly has modified the pristine composition of the magma in equilibrium with its mantle source. The net effect is the increase of the incompatible element content in the calculated rock compositions. For this reason, a new set of data is reported in the same figure (light blue-filled circles), calculated assuming qualitatively the effects of 20% fractionation of a cumulate fraction with 0% REE budget (Fig. 10; details in Electronic Appendix 6). As consequence, the La

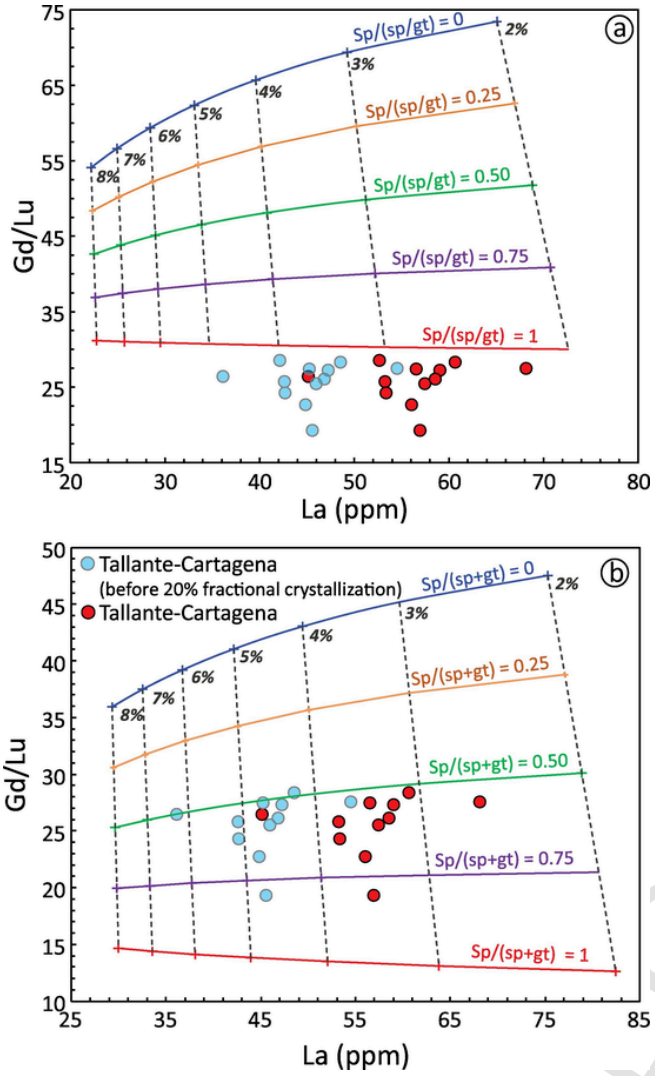

Fig. 10. Gd/La vs. La diagram for the basaltic rocks of Tallante area. Red circles: measured analyses; Light blue circles: measured compositions subtracted 20% of a REE-free cumulate. Red, purple, green, pink and blue lines are batch melting curves of a lithospheric mantle source (McDonough, 1990) with variable spinel/(spinel + garnet) ratio ranging from 1 (red line; only spinel) to zero (blue line; only garnet). The distribution coefficients are from GERM repository system. (a) Partial melting grid assuming the above compositions and distribution coefficients and a modal source peridotite (to calculate P) with 55% olivine, 30% orthopyroxene, 12% clinopyroxene and 3% spinel-garnet. (b) Partial melting grid as before but adding amphibole, leading to a modal source peridotite with 55% olivine, 30% orthopyroxene, 8% clinopyroxene, 3% spinel-garnet and 4% amphibole. Amphibole composition from (Villaseca et al., 2018). The abundance of the minerals entering the melt (to calculate P) is: ~22% olivine, 38% orthopyroxene, 56% clinopyroxene, 13% spinel-garnet, 15% amphibole. All the details reported in the text and in Electronic Appendix 6. (For interpretation of the references to colour in this figure legend, the reader is referred to the web version of this article.)

content in the calculated "primitive" compositions is higher, but Gd/Lu ratios are unchanged, assuming no substantial Gd/Lu fractionation due to olivine (± clinopyroxene) removal.

Assuming anhydrous modal mineralogy and the average lithospheric mantle as source composition, no reliable results can be obtained. Changing the C_0 values with the literature whole-rock composition of the mantle xenoliths found in the Cabezo Negro de Tallante breccia did not improve the result of the modelling. The main problem resides on the calculated Gd/Lu ratios that are always much higher than those of the basaltic rocks. To solve this problem, in Fig. 10b we have reported the results for REE modelling adding 4% of amphibole (composition taken from a peridotite mantle xenolith in Campo de Calatrava lava; Villaseca et al., 2018) to the average lithospheric mantle estimate of McDonough (1990). The modal amount of minerals in the mantle source (to calculate D) is 55:30:8:3:4 for ol:opx:cpx:sp./gt:amph, and the modal amount of the minerals entering the melt (to calculate P) is 22:38:56:13:15 for the same sequence of minerals. The incongruent melting of amphibole leads to the formation of peritectic clinopyroxene (e.g., Medard et al., 2006), resulting in its modal increment and the reduction from the original 71%, in the model of Baker and Stolper (1994), to 56%.

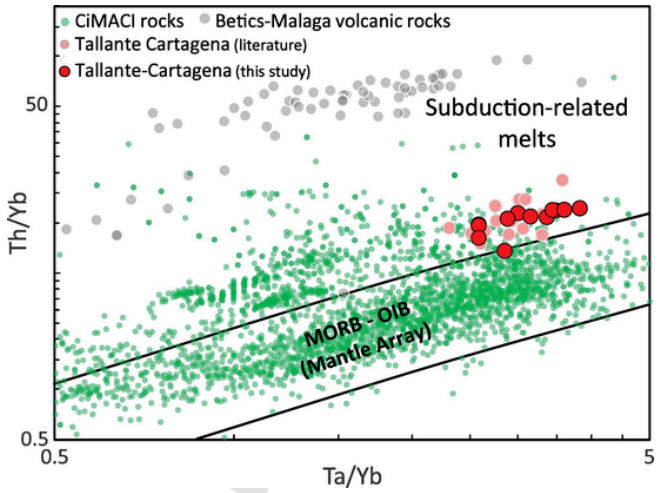

Fig. 11. Th/Yb vs. Ta/Yb diagram for the volcanic products from Cabezo Negro de Tallante and surrounding area. The green dots represent the CiMACI (Circum-Mediterranean Anorogenic Cenozoic Igneous) Province rocks (Lustrino, 2011). (For interpretation of the references to colour in this figure legend, the reader is referred to the web version of this article.)

In this case, the composition of the basaltic rocks plot within the network of calculated melt compositions generated after ~2 to 7% partial melting of a metasomatized, amphibole-bearing lithospheric mantle with a sp./(sp + gt) ratio ranging from 0.75 to 0.50, i.e., in correspondence of the Presnall's cusps close to the lithosphere-asthenosphere boundary (LAB). The transition between the spinel and the garnet phase occurs at a depth of ~60–90 km (e.g., Ziberna et al., 2013), and their coexistence depends on many parameters, as the composition of the mantle and the temperature. In a fertile mantle, spinel and garnet can coexist until ~120 km, whereas in a depleted harzburgite mantle type they are found until ~180 km (Ziberna et al., 2013). The semi-quantitative REE inversion modelling shown in Fig. 10b highlights a depth for the mantle source that is consistent with the LAB. Albeit being only as a qualitative result at best, the REE inversion modelling is compatible with the typical degrees of partial melting for such kind of alkali basaltic compositions (e.g., Cebriá et al., 2009) and the presence of mantle xenoliths in the spinel facies only.

8.7. Inferences on the degree of fractional crystallization

The variation of the oxides of the major elements, as well as the trace element content has been plotted vs. MgO, together with literature data of Tallante area volcanic rocks (Electronic Appendix 6). These diagrams do not show clear trends and only in a few cases it is possible to identify poor correlations (e.g., Ni and Cr vs. MgO; $R^2 < 0.65$) or poor negative correlations (e.g., Al_2O_3, La, Nb; $R^2 < 0.52$). As outlined before, it is possible that the effects of contamination with crustal and mantle xenoliths are responsible for the data scattering, because their digestion may have modified the original parental to evolved compositions.

Fig. 4 shows selected major oxide variations vs. CaO with a quantitative modelling of fractional crystallization based on mass balance.

Sample TAF36 has been chosen to represent the least differentiated magma composition among the studied samples (the parental magma) and sample TAF34 as the most evolved composition of the dataset presented in this study. The fractionation of ~25.5 wt% of a gabbroic cumulate made up of ~13.2% olivine, ~36.4% clinopyroxene, ~35.6% plagioclase, ~12.1% Ti-magnetite and ~ 2.7% apatite has been calculated using the add-in program Solver in MS Excel software, trying to minimize the sum of the squares of the residuals between the hypothetical evolved composition and the sample with the lowest MgO content analysed in this study (TAF34; Electronic Appendix 6). What emerges is that the fractionation of a gabbroic cumulate can explain at least the gross features of the major oxide variation of the basaltic rocks. The major oxide variations consist in an increase of SiO_2, Al_2O_3, Na_2O and K_2O, coupled with a slight decrease of TiO_2, CaO, MgO and FeO in the residual melt, compatible with the mineral phases effectively observed in thin sections (plagioclase, clinopyroxene, olivine, magnetite and apatite; Fig. 4 and Electronic Appendixes 3 and 6).

The best-fit results are not satisfying, considering that the lowest $\sum^2$ obtained is 3.7 (details in Electronic Appendix 6). Going into detail, the strongest bias between the calculated melt and the target composition found for Na_2O (1.46%) and K_2O (0.98%), while for the rest of the major oxides a good match is observed. On this ground, considering the alkali mobility in igneous systems and the scattered variation of these oxides in literature samples too, the mass balance result is here considered as a good qualitative estimate.

8.8. Mantle source characteristics

Cebriá et al. (2009) pointed out that the mantle source that generated the Tallante basaltic magma is characterized by the presence of crustal components, brought to mantle depths as consequence of subduction-related processes. In particular, Cebriá et al. (2009) implied the presence of a component inherited by the same source that produced the Miocene calcalkaline to ultrapotassic volcanic rocks of the Betic Chain. It seems reasonable to think that the mantle sources of the Tallante-Cartagena basaltic magmas still reflect the metasomatic modifications occurred during the previous subduction tectonics, identified in dispersed lithospheric portions once part of a supra-subduction mantle wedge (Cebriá et al., 2009). Evidence for the existence of a lithospheric mantle bearing the effects of a paleo-subduction are indeed found in the mantle xenoliths borne in the basaltic magma (Arai et al., 2003; Avanzinelli et al., 2020; Beccaluva et al., 2004; Bianchini et al., 2011; Hidas et al., 2016). These authors, studying felsic veins in peridotite xenoliths characterized by orthopyroxene reaction margins, made of plagioclase, quartz, amphibole, orthopyroxene and phlogopite, hypothesized the existence of SiO_2-rich metasomatic melts characterized by high $^{176}Hf/^{177}Hf$, $^{87}Sr/^{86}Sr$ and $^{207}Pb/^{204}Pb$ ratios. Such metasomatic melts have identified as old subducted continental crust.

As concerns the ultimate origin of the basaltic activity in the Tallante-Cartagena area, the hypothesis that better fits the data is a sort of edge-driven magmatism (e.g., King and Anderson, 1998). This process consists in a convection flow in a heterogeneous upper mantle. The velocity of the convection and the related magmatic activity would depend on the viscosity and on the lateral temperature gradient between areas with different lithospheric thickness (King and Anderson, 1998). The contact between the thick continental crust of the Iberia Peninsula and the thinner lithosphere of the adjacent back-arc Valencian and Ligurian-Provençal basins of the eastern margin of Spain could be considered as the typical place where edge-driven magmatism can develop.

9. Concluding remarks

A detailed sedimentological, volcanological, petrographic, mineral chemical and geochemical study has been carried out on the Plio-Quaternary pyroclastic breccia and on the basaltic lava flows cropping out in the Tallante-Cartagena volcanic district in SE Spain. Whole-rock geochemistry and Sr-Nd-Pb-O-C isotope investigation carried out on the basaltic portion and the carbonate fraction of the pyroclastic breccias indicate a mixing between a basaltic end-member and a sedimentary component in the form of calcrete-caliche indurated crust. The volcanological, sedimentological, petrographic, mineralogical and geochemical arguments presented in this study are alternative to the hypothesis of the presence of a carbonatitic component as recently proposed for the Cabezo Negro de Tallante by Toscani et al. (2020).

The basaltic scoriae embedded in the breccias are indistinguishable from the lava flow samples. The composition of the basaltic melts is too rich in SiO_2 and too low in alkali to encounter the silicate-carbonate solvus and, consequently, a carbonatite melt separation by immiscibility is considered highly unlike. The identification of biogenic calcrete related to microbial, root and fungi activity, clearly outlines a continental origin for the carbonate matrix that agglutinate the breccias. Moreover, the presence of coated grains, with concentric laminae of $CaCO_3$ around pre-existing silicate clasts, indicates that the scoriae and the carbonate matrix are not genetically related, being the precipitation of the $CaCO_3$ phase subsequent to the emplacement of the volcanic deposit.

The nearly perfect correlation of several geochemical parameters strongly suggests a mechanical process that mixed variable amounts of basaltic rocks (from ~50 to ~90% of the breccia) with a carbonate component accumulated as consequence of variation in the aquifer table in a vadose zone. The nearly sterile composition of the carbonate fraction, extremely poor in both compatible and incompatible elements, their radiogenic $^{87}Sr/^{86}Sr$, unradiogenic $^{143}Nd/^{144}Nd$, the heavy oxygen ($\delta^{18}O_{SMOW}$ from +25.5 to +28.3‰) and light carbon isotopic ratios ($\delta^{13}C_{PDB}$ from −5.9 to −9.9‰) is fully consistent with the proposed model.

In conclusion, we interpret the whole-rock composition of the pyroclastic breccias as the result of mechanical mixing between "normal" basaltic rocks (with the associated abundant mantle and crustal xenolith cargo) and sedimentary carbonates. The presence of upper mantle xenoliths characterized by a dense network of calcite veins and patches is not to be interpreted as the existence of a carbonatitic magma at mantle depths. Rather, it simply represents the results of infiltration of bicarbonate-rich solutions that precipitated calcite in an already emplaced Strombolian pyroclastic deposit characterized in-situ fragmentation of mantle xenolith-rich mildly alkaline volcanic rocks.

The origin of the silicate magma is related to the complex geodynamic and geological evolution of South East Iberia. Here the multitude of tectono-magmatic events that influenced the Iberian plate are reflected on the magmatism that characterized the peninsula, being the resulting underneath lithospheric mantle largely heterogeneous (Bianchini et al., 2011; Cebriá et al., 2009; Doblas et al., 2007). Primitive mantle-normalised diagrams are typical for intra-plate sodic mildly alkaline basaltic compositions. Nevertheless, some anomalies such as the enrichment in LILE (e.g., Th, K) coupled with the presence of radiogenic $^{87}Sr/^{86}Sr$ share some similarities with magmas generated in subduction settings. These intermediate compositions between typical intra-plate and subduction-related melts, lead to the conclusion that the mantle source has been influenced by a paleo-subduction modification, likely identified in the recent Apennine-Maghrebide orogenic phase.

Declaration of Competing Interest

The authors declare that they have no known competing financial interests or personal relationships that could have appeared to influence the work reported in this paper.

The authors declare the following financial interests/personal relationships which may be considered as potential competing interests:

Acknowledgements

Marcello Serracino and Marco Albano are warmly thanked for their usual professional assistance during EMP and SEM investigation. Thanks are also due to Domenico Mannetta for the professional preparation of the thin sections. The detailed review of Vladislav Rapprich (Praha) and of anonymous reviewer greatly improved the quality and readability of the text. The authors thank the Editor Michael Roden for the scientific handling. Ateneo La Sapienza grants (2017-2018-2019) and IGG-CNR fund PCT61 are deeply acknowledged.

Appendix A. Supplementary data

Supplementary data to this article can be found online at https://doi.org/10.1016/j.lithos.2021.106140.

References

[Alonso-Zarza and Arenas, 2004] A.M. Alonso-Zarza, C. Arenas, Cenozoic calcretes from the Teruel Graben, Spain: microstructure, stable isotope geochemistry and environmental significance, Sediment. Geol. 167 (2004) 91–108.

[Alonso-Zarza and Wright, 2010] A.M. Alonso-Zarza, V.P. Wright, Calcretes, in: A.M. Alonso-Zarza, L.H. Tanner (Eds.), Carbonates in Continental Settings, Geochemestry, Diagenesis and Applications, Developments in sedimentology, 62, Elsevier, 2010, pp. 225–267.

[Alonso-Zarza et al., 1998] A.M. Alonso-Zarza, P.G. Silva, J.L. Goy, C. Zazo, Fan-surface dynamics and biogenic calcrete development: interactions during ultimate phases of fan evolution in the semiarid SE Spain (Murcia), Geomorphology 24 (1998) 147–167.

[Alonso-Zarza et al., 2020] A.M. Alonso-Zarza, Á. Rodríguez-Berriguete, A. Martín-Pérez, R. Martín-García, I. Menéndez, J. Mangas, Unravelling calcrete environmental controls in volcanic islands, Gran Canaria Island, Spain, Palaeogeogr. Palaeoclimatol. Palaeoecol. 554 (2020) 109797.

[Arai et al., 2003] S. Arai, Y. Shimizu, F. Gervilla, Quartz diorite veins in a peridotite xenolith from Tallante, Spain: implications for reaction and survival of slab-derived SiO_2-oversaturated melt in the upper mantle, Proce. Japan Acad. Seri. B 79 (2003) 145–150.

[Augier and Jolivet, 2005] R. Augier, L. Jolivet, Late orogenic doming in the eastern Betic Cordilleras: final exhumation of the Nevado-Filabride complex and its relation to basin genesis, Tectonics 24 (2005) TC4003, doi:10.1029/2004TC001687.

[Avanzinelli et al., 2020] R. Avanzinelli, G. Bianchini, M. Tiepolo, A. Jasim, C. Natal, E. Braschi, L. Dallai, L. Beccaluva, S. Conticelli, Subduction-related hybridization of the lithospheric mantle revealed by trace element and Sr-Nd-Pb isotopic data in composite xenoliths from Tallante (Betic Cordillera, Spain), Lithos 352 (2020) 1–17.

[Bailey et al., 2005] K. Bailey, M. Garson, S. Kearns, A.P. Velasco, Carbonate volcanism in Calatrava, Central Spain: a report on the initial findings, Mineral. Mag. 69 (2005) 907–915.

[Baker and Stolper, 1994] M.B. Baker, E.M. Stolper, Determining the composition of high-pressure mantle melts using diamond aggregates, Geochim. Cosmochim. Acta 58 (1994) 2811–2827.

[Bardaji et al., 1995] T. Bardaji, P.G. Silva, J.L. Goy, N.A. Morner, C. Zazo, L. Somoza, C.J. Dabrio, J. Baena, Unchanging environmental conditions during the "Villafranchian" time-span in littoral basins (Eastern Betics, SE Spain), Italian J. Quat. Sci. 8 (1995) 383–390.

[Beccaluva et al., 2004] L. Beccaluva, G. Bianchini, C. Bonadiman, F. Siena, C. Vaccaro, Coexisting anorogenic and subduction-related metasomatism in mantle xenoliths from the Betic Cordillera (southern Spain), Lithos 75 (2004) 67–87.

[Bellon et al., 1983] H. Bellon, P. Bordet, C. Montenat, Chronologie du magmatisme néogène des Cordillères bétiques (Espagne méridionale), Bulletin de la Société Géologique de France 7 (1983) 205–217.

[Benito et al., 1999] R. Benito, J. López-Ruiz, J.M. Cebriá, J. Hertogen, M. Doblas, R. Oyarzun, D. Demaiffe, Sr and O isotope constraints on source and crustal contamination in the high-K calc-alkaline and shoshonitic Neogene volcanic rocks of SE Spain, Lithos 46 (1999) 773–802.

[Bianchini et al., 2011] G. Bianchini, L. Beccaluva, G.M. Nowell, D.G. Pearson, F. Siena, Mantle xenoliths from Tallante (Betic Cordillera): insights into the multi-stage evolution of the south Iberian lithosphere, Lithos 124 (2011) 308–318.

[Brooker, 1998] R.A. Brooker, The effect of CO_2 saturation on immiscibility between silicate and carbonate liquids: an experimental study, J. Petrol. 39 (1998) 1905–1915.

[Brooker and Kjarsgaard, 2011] R.A. Brooker, B.A. Kjarsgaard, Silicate–carbonate liquid immiscibility and phase relations in the system SiO_2-Na_2O-Al_2O_3-CaO-CO_2 at 0.1–2.5 GPa with applications to carbonatite genesis, J. Petrol. 52 (2011) 1281–1305.

[Bustillo and Alonso-Zarza, 2007] M.A. Bustillo, A.M. Alonso-Zarza, Overlapping of and meteoric diagenesis in distal alluvial and shallow lacustrine deposits in the Madrid Miocene Basin, Spain, Sediment. Geol. 198 (2007) 255–271.

[Capedri et al., 1989] S. Capedri, G. Venturelli, E. Salvioli-Mariani, A.J. Crawford, M. Barbieri, Upper-mantle xenoliths and megacrysts in an alkali basalt from Tallante, south-eastern Spain, Eur. J. Mineral. 1 (1989) 685–700.

[Carminati et al., 2012] E. Carminati, M. Lustrino, C. Doglioni, Geodynamic evolution of the central and western Mediterranean: Tectonics vs. igneous petrology constraints, Tectonophysics 579 (2012) 173–192.

[Casciello et al., 2015] E. Casciello, M. Fernàndez, J. Vergés, M. Cesarano, M. Torne, The Alboran Domain in the Western Mediterranean evolution: the birth of a concept, Bulletin de La Société Géologique de France 186 (2015) 371–384.

[Cebriá et al., 2009] J.M. Cebriá, J. López-Ruiz, J. Carmona, M. Doblas, Quantitative petrogenetic constraints on the Pliocene alkali basaltic volcanism of the SE Spain Volcanic Province, J. Volcanol. Geotherm. Res. 185 (2009) 172–180.

[Chakhmouradian, 2006] A.R. Chakhmouradian, High-field-strength elements in carbonatitic rocks: geochemistry, crystal chemistry and significance for constraining the sources of carbonatites, Chem. Geol. 235 (2006) 138–160.

[Chiquet et al., 1999] A. Chiquet, A. Michard, D. Nahon, B. Hamelin, Atmospheric input vs in situ weathering in the genesis of calcretes: an Sr isotope study at Galvez (Central Spain), Geochim. Cosmochim. Acta 63 (1999) 311–323.

[Conticelli et al., 2009] S. Conticelli, L. Guarnieri, A. Farinelli, M. Mattei, R. Avanzinelli, G. Bianchini, E. Boari, S. Tommasini, M. Tiepolo, D. Prelevic, G. Venturelli, Trace elements and Sr–Nd–Pb isotopes of K-rich, shoshonitic, and calc-alkaline magmatism of the Western Mediterranean Region: genesis of ultrapotassic to calc-alkaline magmatic associations in a post-collisional geodynamic setting, Lithos 107 (2009) 68–92.

[Contini et al., 1993] S. Contini, G. Venturelli, L. Toscani, S. Capedri, M. Barbieri, Cr-Zr-armalcolite-bearing lamproites of Cancarix, SE Spain, Mineral. Mag. 57 (1993) 203–216.

[Coulon et al., 2002] C. Coulon, M.H. Megartsi, S. Fourcade, R.C. Maury, H. Bellon, A. Louni-Hacini, J. Cotten, A. Coutelle, D. Hermitte, Post-collisional transition from calc-alkaline to alkaline volcanism during the Neogene in Oranie (Algeria): magmatic expression of a slab breakoff, Lithos 62 (2002) 87–110.

[Dabrio et al., 1991] C.J. Dabrio, Cardeña C. Zazo, J.L. Goy Goy, C. Santisteban Bové, T. Bardají Azcárate, L. Somoza Losada, Neogene and Quaternary fan-delta deposits in southeastern Spain. Field Guide, Cuadernos de Geología Ibérica (1991) 327–400.

[Doblas et al., 2007] M. Doblas, J. López-Ruiz, J.M. Cebriá, Cenozoic evolution of the Alboran Domain: a review of the tectonomagmatic models, in: L. Beccaluva, G. Bianchini, M. Wilson (Eds.), Volcanism in the Mediterranean Area. Geological Society of America, 418, 2007, pp. 303–320.

[Duggen et al., 2004] S. Duggen, K. Hoernle, P. van den Bogaard, C. Harris, Magmatic evolution of the Alboran region: the role of subduction in forming the western Mediterranean and causing the Messinian Salinity Crisis, Earth Planet. Sci. Lett. 218 (2004) 91–108.

[Duggen et al., 2005] S. Duggen, K. Hoernle, P. van den Bogaard, D. Garbe-Schönberg, Post-collisional transition from subduction-to intraplate-type magmatism in the westernmost Mediterranean: evidence for continental-edge delamination of subcontinental lithosphere, J. Petrol. 46 (2005) 1155–1201.

[Faccenna et al., 2014] C. Faccenna, T.W. Becker, L. Auer, A. Billi, L. Boschi, J.P. Brun, F.A. Capitanio, F. Funiciello, F. Horvàth, L. Jolivet, C. Piromallo, L. Royden, F. Rossetti, E. Serpelloni, Mantle dynamics in the Mediterranean, Rev. Geophys. 52 (2014) 283–332.

[Favre and Stampfli, 1992] P. Favre, G.M. Stampfli, From rifting to passive margin: the examples of the Red Sea, Central Atlantic and Alpine Tethys, Tectonophysics 215 (1992) 69–97.

[Fernández Soler, 1996] J.M. Fernández Soler, El volcanismo calco-alcalino en el Parque Natural de Cabo de Gata–Níjar (Almería): Estudio volcanológico y Petrológico, Sociedad Almeriense de Historia

Natural–Consejería de Medio Ambiente de la Junta de Andalucía, Sevilla, 295, 1996.
[García, 1988] C.C. García, Los glacis del Campo de Cartagena, Papeles de Geografía 14 (1988) 35–49.
[García-Hernández et al., 1980] M. García-Hernández, A.C. López-Garrido, P. Rivas, C. Sanz de Galdeano, J.A. Vera, Mesozoic palaeogeographic evolution of the external zones of the Betic Cordillera, Geol. Mijnb. 59 (1980) 155–168.
[Geiger, 1970] F. Geiger, Die Ariditat in Sudostpunien, Stuttgartter Geographische Studien, Band 77 (1970) 1–173.
[Gill et al., 2004] R.C.O. Gill, A. Aparicio, M. El Azzouzi, J. Hernandez, M.F. Thirlwall, J. Bourgois, G.F. Marriner, Depleted arc volcanism in the Alboran Sea and shoshonitic volcanism in Morocco: geochemical and isotopic constraints on Neogene tectonic processes, Lithos 78 (2004) 363–388.
[Goy and Zazo, 1989] J.L. Goy, C. Zazo, The role of neotectonics in the morphologic distribution of the Quaternary marine and continental deposits of the Elche Basin, Southeast Spain, Tectonophysics 163 (1989) 219–225.
[Goy et al., 1990] J.L. Goy, C. Zazo, L. Somoza, C.J. Dabrio, Evolución paleogeográfica de la depresión de Elche-Bajo Segura durante el Pleistoceno, Estud. Geol. 46 (1990) 237–244.
[Gozzi et al., 2014] F. Gozzi, M. Gaeta, C. Freda, S. Mollo, T. Di Rocco, F. Marra, L. Dallai, A. Pack, Primary magmatic calcite reveals origin from crustal carbonate, Lithos 190 (2014) 191–203.
[Grossman, 2012] E.L. Grossman, Oxygen isotope stratigraphy, in: F.M. Gradstein, J.G. Ogg, M.D. Schmitz, G.M. Ogg (Eds.), The geological time scale 2012, 2012, pp. 181–206.
[Guerrera et al., 2019] F. Guerrera, M. Martín-Martín, M. Tramontana, Evolutionary geological models of the central-western peri-Mediterranean chains: a review, Int. Geol. Rev. (2019) 1–22.
[Hamidi et al., 2001] E.M. Hamidi, F. Colin, A. Michard, B. Boulangé, D. Nahon, Isotopic tracers of the origin of Ca in a carbonate crust from the Middle Atlas, Morocco, Chem. Geol. 176 (2001) 93–104.
[Hammouda and Keshav, 2015] T. Hammouda, S. Keshav, Melting in the mantle in the presence of carbon: Review of experiments and discussion on the origin of carbonatites, Chem. Geol. 418 (2015) 171–188.
[Handy et al., 2010] M.R. Handy, S.M. Schmid, R. Bousquet, E. Kissling, D. Bernoulli, Reconciling plate-tectonic reconstructions of Alpine Tethys with the geological–geophysical record of spreading and subduction in the Alps, Earth Sci. Rev.Earth-Sci. Rev. 102 (2010) 121–158.
[Hegner et al., 2020] E. Hegner, S. Rajesh, M. Willbold, D. Müller, M. Joachimski, M. Hofmann, U. Linnemann, J. Zieger, A.P. Pradeepkumar, Sediment-derived origin of the putative Munnar carbonatite, South India, J. Asian Earth Sci. 200 (2020) 104432.
[Hidas et al., 2016] K. Hidas, Z. Konc, C.J. Garrido, A. Tommasi, A. Vauchez, J.A. Padrón-Navarta, C. Marchesi, G. Booth-Rea, A. Acosta-Vigil, C. Szabò, M.I. Varas-Reus, F. Gervilla, Flow in the western Mediterranean shallow mantle: Insights from xenoliths in Pliocene alkali basalts from SE Iberia (eastern Betics, Spain), Tectonics 35 (2016) 2657–2676.
[Humphreys et al., 2010] E.R. Humphreys, K. Bailey, C.J. Hawkesworth, F. Wall, J. Najorka, A.H. Rankin, Aragonite in olivine from Calatrava, Spain — evidence for mantle carbonatite melts from > 100 km depth, Geology 38 (2010) 911–914.
[King and Anderson, 1998] S.D. King, D.L. Anderson, Edge-driven convection, Earth Planet. Sci. Lett. 160 (1998) 289–296.
[King et al., 2020] A.J. King, K.J.H. Phillips, S. Strekopytov, C. Vita-Finzi, S.S. Russell, Terrestrial modification of the Ivuna meteorite and a reassessment of the chemical composition of the CI type specimen, Geochim. Cosmochim. Acta. 268 (2020) 73–89.
[Kjarsgaard, 1998] B.A. Kjarsgaard, Phase relations of a carbonated high-CaO nephelinite at 0.2 and 0.5 GPa, J. Petrol. 39 (1998) 2061–2075.
[Le Maitre, 2002] R.W. Le Maitre, Classification of igneous rocks and glossary of terms, Recommendations of the IUGS Subcommission on the Systematics of Igneous Rocks, Cambridge University Press, 2002.
[Lee et al., 2000] W.J. Lee, W.L. Huang, P. Wyllie, Melts in the mantle modeled in the system CaO-MgO-SiO_2-CO_2 at 2.7 GPa, Contrib. Mineral. Petrol. 138 (2000) 199–213.
[Litasov and Shatskiy, 2018] K.D. Litasov, A. Shatskiy, Carbon-bearing magmas in the Earth's deep interior, in: Y. Kono, C. Sanloup (Eds.), Magma Under Pressure, Elsevier, 2018, pp. 43–82.
[Lustrino, 2000] M. Lustrino, Volcanic activity from the Neogene to the present evolution of the Western Mediterranean area. A review, Ofioliti 25 (2000) 87–101.
[Lustrino, 2011] M. Lustrino, What 'anorogenic' igneous rocks can tell us about the chemical composition of the upper mantle: case studies from the circum-Mediterranean area, Geol. Mag. 148 (2011) 304–316.
[Lustrino and Wilson, 2007] M. Lustrino, M. Wilson, The circum-Mediterranean anorogenic Cenozoic igneous province, Earth Sci. Rev.Earth-Sci. Rev. 81 (2007) 1–65.
[Lustrino et al., 2009] M. Lustrino, V. Morra, L. Fedele, L. Franciosi, Beginning of the Apennine subduction system in central western Mediterranean: constraints from Cenozoic "orogenic" magmatic activity of Sardinia, Italy, Tectonics 28 (2009) 1–23.
[Lustrino et al., 2011] M. Lustrino, S. Duggen, C.L. Rosenberg, The Central-Western Mediterranean: anomalous igneous activity in an anomalous collisional tectonic setting, Earth Sci. Rev.Earth-Sci. Rev. 104 (2011) 1–40.
[Lustrino et al., 2016] M. Lustrino, D. Prelević, S. Agostini, M. Gaeta, T. Di Rocco, V. Stagno, L.S. Capizzi, Ca-rich carbonates associated with ultrabasic-ultramafic melts: Carbonatite or limestone xenoliths? A case study from the late Miocene Morron de Villamayor volcano (Calatrava Volcanic Field, Central Spain), Geochim. Cosmochim. Acta 185 (2016) 477–497.
[Lustrino et al., 2017] M. Lustrino, L. Fedele, S. Agostini, G. Di Vincenzo, V. Morra, Eocene-Miocene igneous activity in Provence (SE France): $^{40}Ar/^{39}Ar$ data, geochemical-petrological constraints and geodynamic implications, Lithos 288 (2017) 72–90.
[Lustrino et al., 2019] M. Lustrino, N. Luciani, V. Stagno, Fuzzy petrology in the origin of carbonatitic/pseudocarbonatitic Ca-rich ultrabasic magma at Polino (Central Italy), Sci. Rep 9 (2019) 1–14.
[Lustrino et al., 2020] M. Lustrino, S. Ronca, A. Caracausi, C.V. Bordenca, S. Agostini, D.B. Faraone, Strongly SiO_2-undersaturated, CaO-rich kamafugitic Pleistocene magmatism in Central Italy (San Venanzo volcanic complex) and the role of shallow depth limestone assimilation, Earth Sci. Rev.Earth-Sci. Rev. 103256 (2020).
[Lustrino et al., 2021] M. Lustrino, G. Salari, B. Rahimzadeh, L. Fedele, F. Masoudi, S. Agostini, Quaternary melanephelinites from Nowbaran (NW Urumieh-Dokhtar Magmatic Arc, Iran): origin of ultrabasic-ultracalcic melts in a post-collisional setting, J. Petrol. (2021).
[Lyubetskaya and Korenaga, 2007] T. Lyubetskaya, J. Korenaga, Chemical composition of Earth's primitive mantle and its variance: 1. Method and results, J. Geophys. Res. Solid Earth 112 (2007) 1–21.
[Manteca et al., 2016] J.I. Manteca, J. López-Ruiz, J.M. Cebriá, El campo volcánico del oeste de Cartagena y su importancia patrimonial. En Francisco Belmonte Serrano, Gustavo A, in: Ballesteros Pelegrín, Jorge M. Sánchez Balibrea, A. Daniel Ibarra Marinas (Eds.), Cuestiones sobre Paisaje, Patrimonio Natural y Medio Ambiente en el Sureste Ibérico, Ediciones de la Universidad de Murcia, 2016, pp. 56–64.
[Martin et al., 2013] L.H.J. Martin, M.W. Schmidt, H.B. Mattsson, D. Günther, Element partitioning between immiscible carbonatite and silicate melts for dry and H_2O-bearing systems at 1-3 GPa, J. Petrol. 54 (2013) 2301–2338.
[Mather et al., 2019] C.C. Mather, D.J. Nash, S. Dogramaci, P.F. Grierson, G. Skrzypek, Geomorphic and hydrological controls on groundwater dolocrete formation in the semi-arid Hamersley Basin, Northwest Australia, Earth Surf. Process. Landf. 44 (2019) 2752–2770.
[Mattei et al., 2014] M. Mattei, N.R. Riggs, G. Giordano, L. Guarnieri, F. Cifelli, C.C. Soriano, B. Jicha, A. Jasim, S. Marchionni, L. Franciosi, S. Tommasini, M. Porreca, S. Conticelli, Geochronology, geochemistry and geodynamics of the Cabo de Gata volcanic zone, Southeastern Spain, Ital. J. Geosci. 133 (2014) 341–361.
[McDonough, 1990] W.S. McDonough, Constraints on the composition of the continental lithospheric mantle, Earth Planet. Sci. Lett. 101 (1990) 1–18.
[Medard et al., 2006] E. Medard, M.W. Schmidt, P. Schiano, L. Ottolini, Melting of amphibole-bearing wehrlites: an experimental study on the origin of ultra-calcic nepheline-normative melts, J. Petrol. 47 (2006) 481–504.
[Meijninger and Vissers, 2006] B.M.L. Meijninger, R.L.M. Vissers, Miocene extensional basin development in the Betic Cordillera, SE Spain revealed through analysis of the Alhama de Murcia and Crevillente Faults, Basin Res. 18 (2006) 547–571.
[Montenat and d'Estevou, 1999] C. Montenat, P.O. d'Estevou, The diversity of late Neogene sedimentary basins generated by wrench faulting in the eastern Betic Cordillera, SE Spain, J. Pet. Geol. 22 (1999) 61–80.
[Munksgaard, 1984] N.C. Munksgaard, High $\delta^{18}O$ and possible pre-eruptional Rb-Sr isochrons in cordierite-bearing Neogene volcanics from SE Spain, Contrib. Mineral. Petrol. 87 (1984) 351–358.
[Nabyl et al., 2020] Z. Nabyl, M. Massuyeau, F. Gaillard, J. Tuduri, G. Iacono-Marziano, G. Rogerie, E. Le Trong, I. Di Carlo, J. Melleton, L. Bailly, A window in the course of alkaline magma differentiation conductive to immiscible REE-rich carbonatites, Geochim. Cosmochim. Acta 282 (2020) 297–323.
[Nelson et al., 1986] D.R. Nelson, M.T. McCulloch, S.S. Sun, The origins of ultrapotassic rocks as inferred from Sr, Nd and Pb isotopes, Geochim. Cosmochim. Acta 50 (1986) 231–245.
[Nixon et al., 1984] P.H. Nixon, F. Thirlwall, F. Buckley, C.J. Davies, Spanish and western Australian lamproites: Aspects of whole rock geochemistry, in: J. Kornprobst (Ed.), Kimberlites and Related Rocks, Elsevier, Amsterdam, 1984, pp. 285–296.
[Peccerillo, 2004] A. Peccerillo, Carbonate-rich pyroclastic rocks from central Apennines: carbonatites or carbonated rocks? A commentary, Mineral. Petrol. 73 (2004) 165–175.
[Pedrera et al., 2010] A. Pedrera, J. Galindo-Zaldívar, A. Tello, C. Marín-Lechado, Intramontane basin development related to contractional and extensional structure interaction at the termination of a major

sinistral fault: the Huércal-Overa Basin (Eastern Betic Cordillera), J. Geodyn. 49 (2010) 271–286.
[Pérez-Valera et al., 2013] L.A. Pérez-Valera, G. Rosenbaum, M. Sánchez-Gómez, A. Azor, J.M. Fernández-Soler, F. Pérez-Valera, P.M. Vasconcelos, Age distribution of lamproites along the Socovos Fault (southern Spain) and lithospheric scale tearing, Lithos 180 (2013) 252–263.
[Poli, 2016] S. Poli, Melting carbonated eclogites: carbonatites from subducting slabs, Progr. Earth Planet. Sci. 3 (2016) 27, doi:10.1186/s40645-016-0105-6.
[Puga et al., 2011] E. Puga, M. Fanning, A.D. de Federico, J.M. Nieto, L. Beccaluva, G. Bianchini, M.A.D. Puga, Petrology, geochemistry and U-Pb geochronology of the Betic Ophiolites: inferences for Pangaea break-up and birth of the westernmost Tethys Ocean, Lithos 124 (2011) 255–272.
[Romero and Belmonte, 2011] Díaz A. Romero, Serrato F. Belmonte, El Campo de Cartagena una visión global, Recorridos por el Campo de Cartagena. Control de la degradación y uso sostenible del suelo. Murcia, Instituto Mediterráneo del Agua, 2011, pp. 17–48.
[Rosello Verger, 1970] V.M. Rosello Verger, Clima y morfología pleistocena en el litoral mediterráneo español, Papeles de Geografía 2 (1970) 79–108.
[Samoza et al., 1989] L. Samoza, C. Zazo, J.L. Goy, N.A. Morner, Estudio geomorfologico de secuencias de abanicos aluviales cuaternarios (Alicante-Murcia, Esapaña), Cuaternario y Geomorfologia 3 (1989) 73–82.
[Santosh et al., 1987] M. Santosh, P.K. Thampi, S.S. Iyer, M.B.A. Vasconcellos, Rare earth element geochemistry of Munnar carbonatite, Central Kerala, J. Geol. Soc. India 29 (1987) 335–343.
[Sanz De Galdeano, 1990] C. Sanz De Galdeano, Geologic evolution of the Betic Cordilleras in the Western Mediterranean, Miocene to the present, Tectonophysics 172 (1990) 107–119.
[Schmidt and Weidendorfer, 2018] M.W. Schmidt, D. Weidendorfer, Carbonatites in oceanic hotspots, Geology 46 (2018) 435–438.
[Shaw, 1970] D.M. Shaw, Trace element fractionation during anatexis, Geochim. Cosmochim. Acta 34 (1970) 237–243.
[Shaw, 2018] C.S.J. Shaw, Evidence for the presence of carbonate melt during the formation of cumulates in the Colli Albani Volcanic District, Italy, Lithos 310–311 (2018) 105–119.
[Silva et al., 1993] P.G. Silva, J.L. Goy, L. Somoza, C. Zazo, T. Bardajı, Landscape response to strike–slip faulting linked to collisional settings: Quaternary tectonics and basin formation in the East-ern Betics SE Spain, Tectonophysics 224 (1993) 289–303.
[Sissingh, 2008] W. Sissingh, Punctuated Neogene tectonics and stratigraphy of the African-Iberian plate-boundary zone: concurrent development of Betic-Rif basins (southern Spain, northern Morocco), Netherlands J. Geosci. Geologie en Mijnbouw 87 (2008) 241–289.
[Soria et al., 2001] J.M. Soria, P. Alfaro, J. Fernández, C. Viseras, Quantitative subsidence-uplift analysis of the Bajo Segura Basin (eastern Betic Cordillera, Spain): tectonic control on the stratigraphic architecture, Sediment. Geol.Sedimentary Geol. 140 (2001) 271–289.
[Stampfli and Hochard, 2009] G.M. Stampfli, C. Hochard, Plate tectonics of the Alpine realm, Geol. Soc. Lond., Spec. Publ. 327 (2009) 89–111.
[Stampfli and Kozur, 2006] G.M. Stampfli, H.W. Kozur, Europe from the Variscan to the Alpine cycles, Memoirs-of the Geological Society of London, 32, 2006, pp. 57–82.
[Stoppa et al., 2005] F. Stoppa, G. Rosatelli, F. Wall, T. Jeffries, Geochemistry of carbonatite-silicate pairs in nature: a case history from Central Italy, Lithos 85 (2005) 26–47.
[Stoppa et al., 2012] F. Stoppa, G. Rosatelli, M. Schiazza, A. Tranquilli, Hydrovolcanic vs. magmatic processes in forming maars and associated pyroclasts: the Calatrava-Spain-case history, Updates in Volcanology – A Comprehensive Approach to Volcanological Problems, 2012, pp. 3–26.
[Stoppa et al., 2016] F. Stoppa, F. Pirajno, M. Schiazza, N.V. Vladykin, State of the art: Italian carbonatites and their potential for critical-metal deposits, Gondwana Res. 37 (2016) 152–171.
[Tappe et al., 2017] S. Tappe, R.L. Romer, A. Stracke, A. Steenfelt, K.A. Smart, K. Muehlenbachs, T.H. Torsvik, Sources and mobility of carbonate melts beneath cratons, with implications for deep carbon cycling, metasomatism and rift initiation, Earth Planet. Sci. Lett. 466 (2017) 152–167.
[Taylor Jr et al., 1967] H.P. Taylor Jr., J. Frechen, E.T. Degens, Oxygen and carbon isotope studies of carbonatites from the Laacher See District, West Germany and Alnö District, Sweden, Geochim. Cosmochim. Acta 31 (1967) 407–430.
[Torres-Roldán et al., 1986] R.L. Torres-Roldán, G. Poli, A. Peccerillo, An early Miocene arc-tholeiitic magmatic dike event from the Alboran Sea-evidence for precollisional subduction and back-arc crustal extension in the westernmost Mediterranean, Geol. Rundsch. 75 (1986) 219–234.
[Toscani et al., 1990] L. Toscani, G. Venturelli, M. Barbieri, S. Capedri, J.F. Soler, M. Oddone, Geochemistry and petrogenesis of two-pyroxene andesites from Sierra de Gata (SE Spain), Mineral. Petrol. 41 (1990) 199–213.
[Toscani et al., 1995] L. Toscani, S. Contini, M. Ferrarini, Lamproitic rocks from Cabezo Negro de Zeneta: brown micas as a record of magma mixing, Mineral. Petrol. 55 (1995) 281–292.
[Toscani et al., 2020] L. Toscani, E. Salvioli-Mariani, M. Mattioli, C. Tellini, T. Boschetti, P. Iacumin, E. Selmo, The pyroclastic breccia of the Cabezo Negro de Tallante (SE Spain): the first finding of carbonatite volcanism in the Internal Domain of the Betic Cordillera, Lithos 354–355 (2020) 105288.
[Turner et al., 1999] S.P. Turner, J.P. Platt, R.M.M. George, S.P. Kelley, D.G. Pearson, G.M. Nowell, Magmatism associated with orogenic collapse of the Betic-Alboran domain, SE Spain, J. Petrol. 40 (1999) 1011–1036.
[van Hinsbergen et al., 2020] D.J. van Hinsbergen, T.H. Torsvik, S.M. Schmid, L.C. Maţenco, M. Maffione, R.L. Vissers, D. Gurer, W. Spakman, Orogenic architecture of the Mediterranean region and kinematic reconstruction of its tectonic evolution since the Triassic, Gondwana Res. 81 (2020) 79–229.
[Venturelli et al., 1984] G. Venturelli, S. Capedri, G. Di Battistini, A. Crawford, L.N. Kogarko, S. Celestini, The ultrapotassic rocks from southeastern Spain, Lithos 17 (1984) 37–54.
[Vera, 2000] J.A. Vera, El Terciario de la Cordillera Bética: estado actual de conocimientos, Rev. Soc. Geol. Esp. 13 (2000) 345–373.
[Villaseca et al., 2018] C. Villaseca, E.A. Belousova, D.N. Barfod, J.M. González-Jiménez, Dating metasomatic events in the lithospheric mantle beneath the Calatrava volcanic field (Central Spain), Lithosphere 11 (2018) 192–208.
[Wallace and Green, 1988] M.E. Wallace, D.H. Green, An experimental determination of primary magma composition, Nature 335 (1988) 343–346.
[Woolley and Bailey, 2012] A.R. Woolley, D.K. Bailey, The crucial role of lithospheric structure in the generation and release of carbonatites: geological evidence, Mineral. Mag. 76 (2012) 259–270.
[Woolley and Kempe, 1989] A.R. Woolley, D.R.C. Kempe, Carbonatites: Nomenclature, average chemical compositions, and element distribution, in: K. Bell (Ed.), Carbonatites: Genesis and Evolution, Unwyn Hyman, London, 1989, pp. 1–14.
[Woolley and Kjarsgaard, 2008] A.R. Woolley, B.A. Kjarsgaard, Paragenetic types of carbonatite as indicated by the diversity and relative abundances of associated silicate rocks: evidence from a global database, Can. Mineral. 46 (2008) 741–752.
[Wright, 1991] V.P. Wright, Calcretes: an introduction, in: V.P. Wright, M.E. Tucker (Eds.), Calcretes, 1991, pp. 1–22.
[Wright and Tucker, 1991] V.P. Wright, M.E. Tucker, Calcretes: an introduction, in: V.P. Wright, M.E. Tucker (Eds.), Calcrete, International Association of Sedimentologists Special Publication, 2, Blackwell Scientific Publications, Oxford, 1991, pp. 1–21.
[Wyllie and Tuttle, 1960] P.J. Wyllie, O.F. Tuttle, The system CaO-CO_2-H_2O and the origin of carbonatites, J. Petrol. 1 (1960) 1–46.
[Yaxley et al., 2019] G.M. Yaxley, S. Ghosh, E.S. Kiseeva, A. Mallik, C. Spandler, A.R. Thomson, M.J. Walter, CO_2-rich melts in Earth, Deep Carbon: Past to Present, 2019, pp. 129–162.
[Zeck et al., 1999] H.P. Zeck, A.B. Kristensen, E. Nakamura, Inherited Palaeozoic and Mesozoic Rb–Sr Isotopic Signatures in Neogene Calc-alkaline Volcanics, Alborán Volcanic Province, SE Spain, J. Petrol. 40 (1999) 511–524.
[Ziberna et al., 2013] L. Ziberna, S. Klemme, P. Nimis, Garnet and spinel in fertile and depleted mantle: insights from thermodynamic modelling, Contrib. Mineral. Petrol. 166 (2013) 411–421.